



POLITECNICO
MILANO 1863



Anthropogenic Water Use (CCI-AWU)

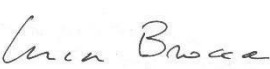
Deliverable 6:

Product Validation and Intercomparison Report (PVIR)

Date	Issue	Section	Page	Comment
18/04/2025	1.0			

Control Document

Process	Name	Date
Written by:	Pierre Lallet, Jacopo Dari, Sara Modanesi, Michel Bechtold, Louise Busschaert Luca Brocca, Christian Massari, Carla Saltalippi, Renato Morbideli, Gabrielle De Lannoy, Zdenko Heyvaert, Wouter Dorigo, Pia Langhans, Maria Cristina Rulli, Davide Danilo Chiarelli, Nikolas Galli	
Checked by	Luca Brocca	18/04/2025

	Signature	Date
For CCI-AWU team		18/04/2025
For ESA		

[This page is left intentionally blank]

List of content

Sommario

1. Introduction.....	5
1.1. The CCI-AWU project.....	5
1. 2. Scope of this report	5
1.3. Applicable documents	6
1.4. Overview of methods and datasets.....	6
1.5. Report content and structure.....	7
2. CONUS	9
2.1. Evaluation with in situ irrigation data	9
2.2. Assessment of spatial patterns.....	11
2.3. Assessment of spatial patterns using auxiliary data	13
2.4. Intercomparison of temporal dynamics	15
3. Ebro Basin	17
3.1. Evaluation with in situ irrigation data	17
3.2. Intercomparison of spatial patterns.....	19
3.3. Assessment of spatial patterns using auxiliary data	20
3.4. Intercomparison of temporal dynamics	20
4. Murray-Darling Basin.....	22
4.1. Evaluation with in situ irrigation data	22
4.2. Intercomparison of spatial patterns.....	26
4.3. Assessment of spatial patterns using auxiliary data	28
4.4. Intercomparison of temporal dynamics	30
5. India	32
5.1. Intercomparison of spatial patterns.....	32
5.2. Assessment of spatial patterns using auxiliary data	34
5.3. Intercomparison of temporal dynamics	35
6. Summary and conclusions	36
Appendix.....	38
References	41

1. Introduction

1.1. The CCI-AWU project

The closure of the Earth's water cycle (as well as the energy balance and the carbon cycles) through satellite Earth Observation (EO) represents one of the outstanding scientific challenges highlighted by the Global Climate Observing System (GCOS). Required standards of accuracy are fixed to 5% and annual timescale. To this end, a suite of essential climate variables (ECVs) has been defined to understand the evolution of climate and to assess the potential derived risks. However, if targets at annual timescale can generally be reached, larger uncertainties are observed for sub-annual and sub-continental time and spatial scales, respectively (Dorigo et al., 2021; Rodell et al., 2015). In this context, the development of an ECV that includes information on anthropogenic water use (AWU) can help in advancing the proper closure of the water cycle at higher spatial and temporal scales. In the ESA Climate Change Initiative Anthropogenic Water Use (CCI-AWU) precursor project, AWU is more specifically intended as agricultural water allocated for irrigation, which represents the largest anthropogenic water use, thus making irrigation the most impactful human activity on the hydrological cycle. The Food and Agricultural Organization of the United Nations (FAO, 2016) estimated that irrigation, worldwide, accounts for more than 70% of water withdrawn from the surface (i.e., rivers, lakes) and subsurface (i.e., groundwater) water sources and these estimates are expected to increase in the near future due to an increase in population and in food production, especially over arid and semi-arid regions (McDermid et al., 2023). In this context, the main data source identified by GCOS for tracking AWU is FAO's AQUASTAT. However, AQUASTAT provides survey-based irrigation estimates that do not meet the GCOS requirements, i.e., data are provided on a 5-year interval instead of yearly and are available every 2-3 years.

The overarching objective of the Climate Change Initiative – Anthropogenic Water Use (CCI-AWU) precursor project is to derive long-term (i.e., at least twenty years) AWU time series for selected regions using several approaches exploiting remote sensing observations, as a proof-of-concept of the feasibility towards a proper AWU ECV product.

The CCI-AWU project is led by a consortium coordinated by CNR-IRPI and includes the following institutions:

1. Vienna University of Technology (TU Wien) (TUWIEN)
2. KU Leuven, Department of Earth and Environmental Sciences, Division of Soil and Water Management (KULeuven)
3. University of Perugia (UNIPG)
4. Politecnico di Milano, Department of Civil and Environmental Engineering (POLIMI)

1. 2. Scope of this report

This document presents an intercomparison of monthly 0.25° irrigation water use datasets produced as part of Work Package 3 (WP3) of the CCI-AWU project. The aim of this report is to complement the validation of the datasets against in situ irrigation data described in the D4 PVSAR by cross-comparing the irrigation datasets with each other and using auxiliary data. The intercomparison includes datasets generated using the SM-based Inversion method (Brocca et al. 2018; Dari et al., 2021, 2022, 2023), referred to as "SM-

INVERSION" in this document, datasets obtained with the SM-based Delta method (Zaussinger et al. 2019; Zappa et al., 2021, 2022, 2024), referred to as "SM-DELTA", and datasets generated using the Model-observation integration approach based on the Noah-MPv4.0.1 land surface model (Niu et al., 2011) coupled to a sprinkler irrigation scheme (Ozdogan et al., 2010) overlaid with irrigated area maps, referred to as "NOAH-MP" hereafter.

1.3. Applicable documents

- Proposal
- Deliverable D2. Report explaining the criteria for selecting the test regions.
- Deliverable D3. Algorithm Theoretical Baseline Document (ATBD).
- Deliverable D4. Product Validation and Algorithm Selection Report (PVASR).
- Deliverable D7. Product User Guide (PUG).

All deliverables mentioned here will be made publicly available at the following link:
<https://climate.esa.int/en/projects/anthropogenic-water-use/>.

1.4. Overview of methods and datasets

The SM-INVERSION method is based on the inversion of the soil water balance model (Brocca et al., 2018; Dari et al., 2023), where all terms are derived from soil moisture (SM) data. The SM-DELTA method is based on the difference in temporal dynamics between the satellite and model SM (and evapotranspiration ET). NOAH-MP irrigation estimates are obtained through an ensemble of land model trajectories composed of 24 ensemble members, generated by perturbing meteorological forcings and overlaid with three different irrigation maps: a Landsat-based irrigated fraction dataset (Teluguntla et al., 2023) referred to as "Landsat"; a dataset based on the Relative Bias Approach (see ATBD Section 5.2.1), referred to as "Method 1"; and another based on the Multi-Resolution Analysis approach (see ATBD Section 5.2.2), referred to as "Method 2". Note that although the NOAH-MP irrigation datasets consist of an ensemble of simulations and thus provide spread (uncertainty) of simulations, in this intercomparison only the ensemble mean values have been analyzed.

The intercomparison focuses on the four key regions of interest identified in the CCI-AWU project, namely the Contiguous United States (CONUS), the Ebro basin in Spain, the Murray-Darling basin in Australia, and India. Table 1 presents an overview of the datasets included in this analysis, along with their time coverage and availability across the four different regions. The terms "CCI Combined," "CCI Passive," and "CCI Active" refer to ESA CCI SM products, while FLUXCOM and SSEBOP refer to ET products used in the SM-DELTA approach.

Table 1: Datasets analyzed with their time coverage and availability for each region. Red indicates unavailable datasets for the region.

Method	Dataset	Data availability	CONUS	Ebro	Murray-Darling	India
SM-DELTA	CCI Combined & FLUXCOM	2003-2020				
	CCI Passive & FLUXCOM	2003-2020				
	CCI Active & FLUXCOM	2003-2020				
	CCI Combined & SSEBOP	2003-2022				
	CCI Passive & SSEBOP	2003-2022				
	CCI Active & SSEBOP	2003-2022				
SM-INVERSION	CCI Combined	2003-2022				
	CCI Passive	2003-2022				
	ASCAT	2003-2022				
	SMOS	2010-2022				
	SMAP	2015-2022				
NOAH-MP	Landsat	2010-2022				
	Method 1	2010-2022				
	Method 2	2010-2022				

1.5. Report content and structure

This document focuses on three key aspects: first, an intercomparison of performance against in situ data; second, an analysis of the spatial consistency of irrigation estimates against auxiliary data, namely the percentage of irrigated area from the Global Map of Irrigated Area (GMIA; Siebert et al., 2013); and third, an intercomparison of irrigation time series. The report is structured as follows: Section 2 presents the analysis

for the CONUS region, section 3 for the Ebro Basin, section 4 for the Murray-Darling Basin, section 5 for India, and section 6 presents a summary and a conclusion.

2. CONUS

2.1. Evaluation with in situ irrigation data

All datasets were analyzed against annual irrigation volume data for each state within CONUS for the years 2013 and 2018, using the Farm and Ranch Irrigation Survey (FRIS) produced by the National Agricultural Statistics Service (NASS) of the United States Department of Agriculture (USDA). The reader can refer to the Deliverable 2 Report Explaining the Criteria for Selecting Test Regions (section 2.3.1), for more detailed information.

Figure 1 summarizes the Root Mean Square Deviation (RMSD), bias, and Pearson correlation coefficient (R) values obtained using the three methods (x-axis), with blue points corresponding to 2013 and orange points to 2018. The black vertical bar indicates the average metric value calculated across all datasets belonging to the same method. Table 2 shows the same information with detailed metric values for each dataset. In this Table, each value is accompanied by a color-coded scale: dark blue highlights the best performance (lowest RMSD and bias, highest Pearson R) among all datasets for a given year, whereas dark red indicates the worst-performing dataset (highest RMSD and bias, lowest Pearson R).

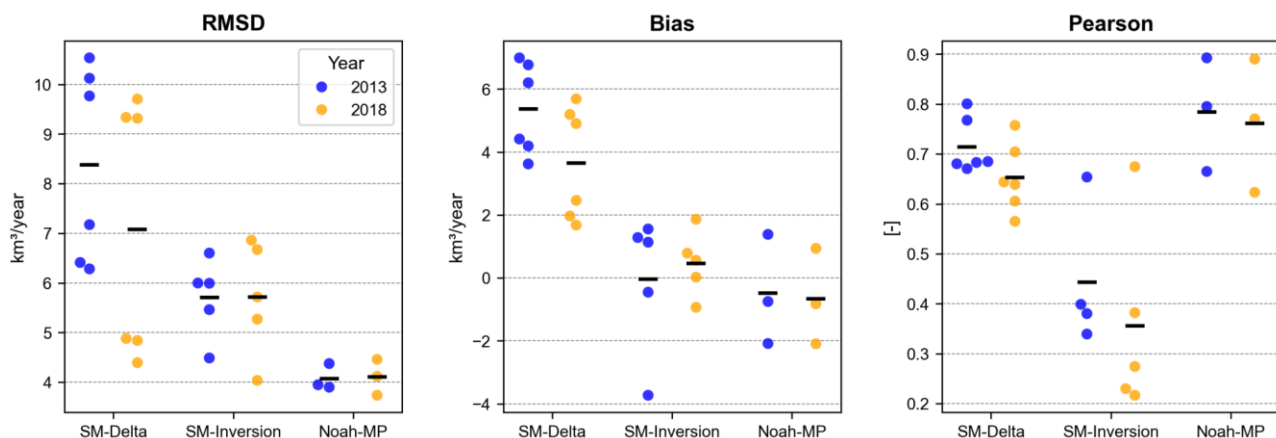


Figure 1: Swarmplot displaying the metric values (RMSD, bias, Pearson R) obtained for the years 2013 (blue) and 2018 (orange) for all datasets derived using the SM-DELTA, SM-INVERSION, and NOAH-MP methods.

For datasets derived using the SM-DELTA method, those including the SSEBOP ET product exhibit significantly higher RMSD (9.80 km³/year on average) and bias (6.0 km³/year on average) compared to all the other datasets. SM-DELTA datasets including the FLUXCOM ET product also show relatively high bias and RMSD values in 2013, but their performance aligns more closely with other datasets in 2018. The Pearson R values tend to be relatively high for datasets integrating FLUXCOM, particularly for the CCI Passive & FLUXCOM datasets. Overall, within the SM-DELTA method, the CCI Passive & FLUXCOM dataset emerges as the best-performing product for CONUS.

For datasets obtained through the SM-INVERSION method, the CCI Passive dataset stands out as the most accurate, with a lower RMSD than other SM-INVERSION datasets, a consistently low bias, and a significantly higher Pearson R value compared to the other datasets obtained with this method.

Regarding the NOAH-MP datasets, they show the highest overall performance across all metrics, with the lowest RMSD and bias and the highest Pearson R values. Among the three NOAH-MP products, the Landsat-based dataset appears to perform slightly better than the others.

The next analyses for the CONUS region will focus on the datasets with the best performance for each method in this region: CCI Passive & FLUXCOM for SM-DELTA, CCI Passive for SM-INVERSION, and Landsat for NOAH-MP.

Table 2: Performance metrics (RMSD, bias, Pearson R) obtained in the CONUS for the years 2013 and 2018 for all datasets derived using the SM-DELTA, SM-INVERSION, and NOAH-MP methods.

Method	Dataset	RMSD (km ³ /y)		Bias (km ³ /y)		Pearson R (-)	
		2013	2018	2013	2018	2013	2018
SM-Delta	CCI Combined & FLUXCOM	6,3	4,8	3,6	1,7	0,68	0,64
	CCI Passive & FLUXCOM	6,4	4,4	4,2	2,0	0,80	0,76
	CCI Active & FLUXCOM	7,2	4,9	4,4	2,5	0,68	0,70
	CCI Combined & SSEBOP	9,8	9,3	6,2	4,9	0,67	0,57
	CCI Passive & SSEBOP	10,1	9,3	6,8	5,2	0,77	0,64
	CCI Active & SSEBOP	10,5	9,7	7,0	5,7	0,68	0,61
SM-Inversion	CCI Combined	6,0	5,7	1,6	0,6	0,34	0,23
	CCI Passive	4,5	4,0	1,3	0,0	0,65	0,67
	ASCAT	6,0	6,9	1,1	1,9	0,38	0,27
	SMOS	5,5	5,3	-0,5	-0,9	0,40	0,38
	SMAP		6,7		0,8		0,22
NOAH-MP	Landsat irrigation map	4,0	3,7	1,4	0,9	0,80	0,77
	"Method 1" irrigation map	4,4	4,5	-0,8	-0,8	0,67	0,62
	"Method 2" irrigation map	3,9	4,1	-2,1	-2,1	0,89	0,89

2.2. Assessment of spatial patterns

Figure 2 presents maps of the three selected datasets, showing the mean annual irrigation for the period they have in common (2010–2020) (Figure 2a). Additionally, scatterplots comparing estimated irrigation (y-axis) with observed values (x-axis) for each dataset, with 2013 represented in blue and 2018 in orange are shown in Figure 2b. The main irrigated regions of CONUS (California Valley, Snake River Plain, Great Plains, and Mississippi Floodplains) are shown in Figure 3a, and a map of surface area equipped for irrigation per 0.25° pixel from GMIA is shown in Figure 3b.

The spatial distribution of irrigation varies significantly across the three datasets. The SM-INVERSION (CCI Passive) dataset exhibits relatively homogeneous values, mostly ranging between 50 and 150 mm/year. In contrast, the SM-DELTA (CCI Passive & FLUXCOM) shows a more heterogeneous pattern, with a clear west-to-east gradient: values in the western regions frequently range from 150 to over 350 mm/year, while areas such as the Mississippi Floodplain typically remain below 150 mm/year. The NOAH-MP (Landsat) dataset presents an even more heterogeneous pattern, with irrigation being highly localized in the most intensively irrigated areas. NOAH-MP (Landsat) also shows a west-to-east gradient, with large portions of the California Valley exceeding 500 mm/year, while the Mississippi Floodplain shows values between 150 and 200 mm/year.

The spatial patterns observed in NOAH-MP (Landsat) are strongly correlated with the percentage of irrigated areas (Figure 3a). This correlation is expected, as NOAH-MP (Landsat) explicitly uses maps of percentage of irrigated area to simulate irrigation (from a Landsat-derived map). In contrast, SM-INVERSION (CCI Passive) and SM-DELTA (CCI Passive & FLUXCOM) datasets apply a mask after the simulations to exclude non-irrigated pixels, using a minimum threshold of 5% equipped irrigation fraction per pixel (from the GMIA map).

Comparison of irrigation datasets in the CONUS (2010-2022)

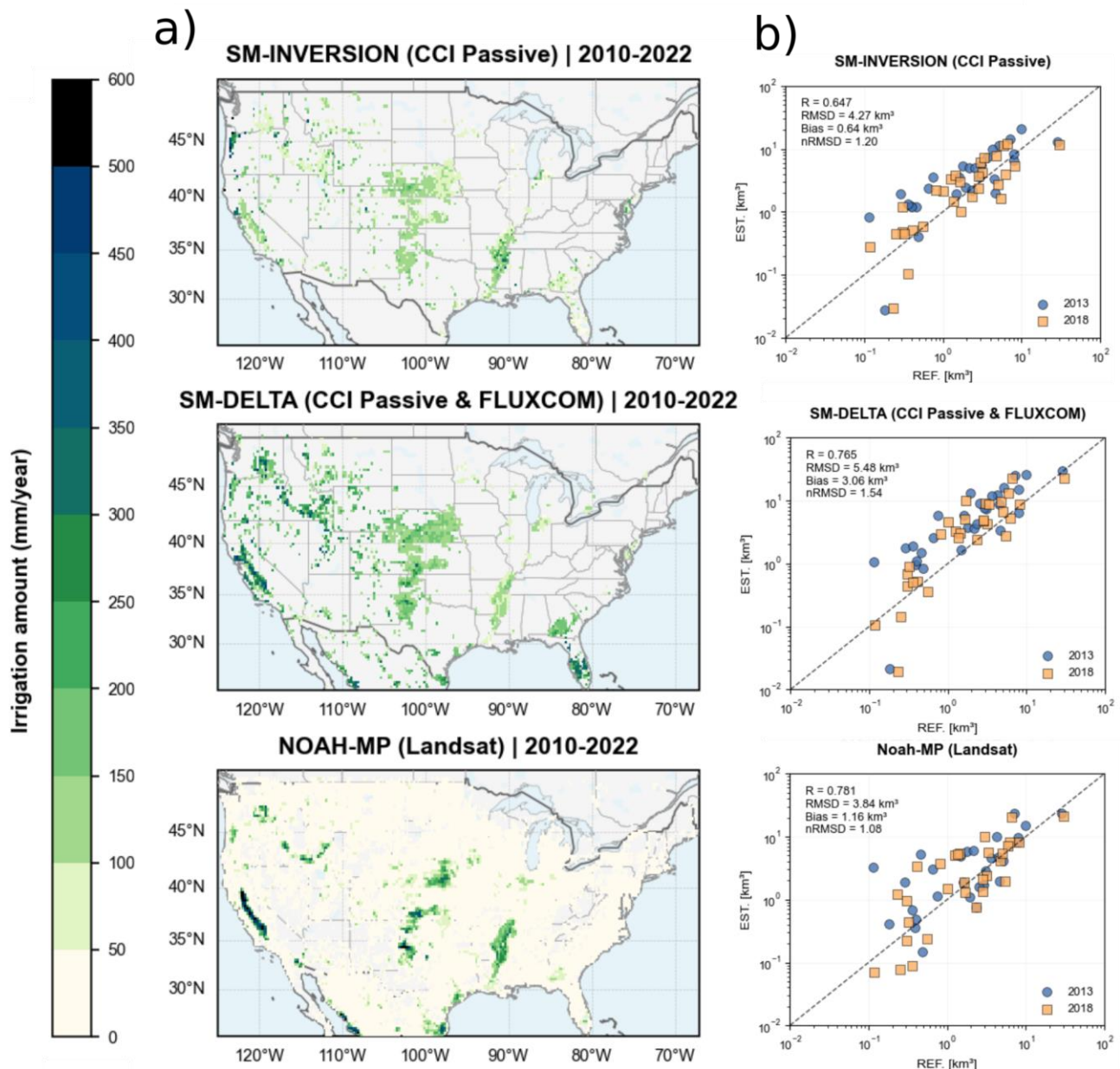


Figure 2: a) Map of mean annual irrigation estimates for SM-INVERSION (CCI Passive), SM-DELTA (CCI Passive & FLUXCOM), and NOAH-MP (Landsat) for the period 2010–2020. b) Scatterplots comparing estimated (y-axis) and observed (x-axis) irrigation for each dataset, with 2013 in blue and 2018 in orange.

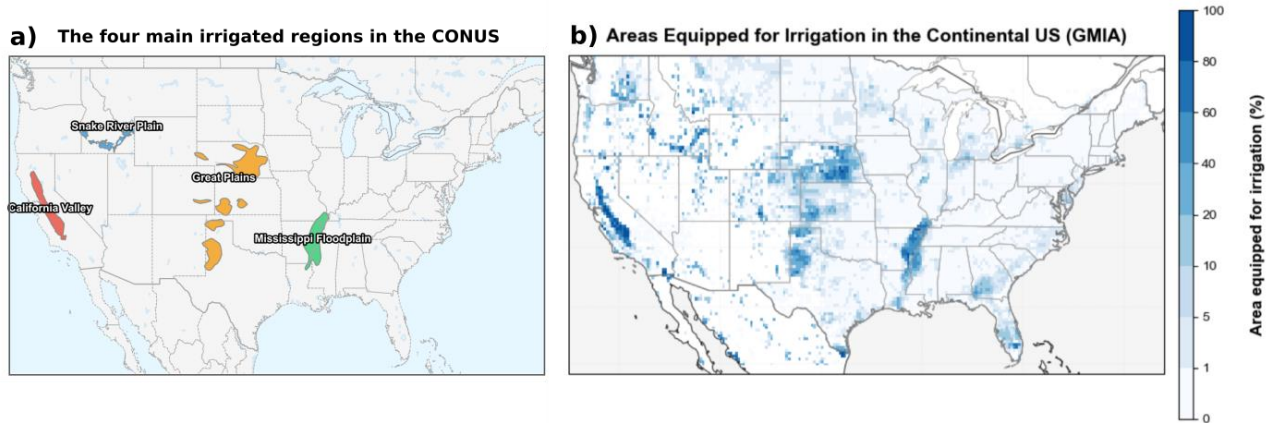


Figure 3: a) The four main irrigated regions of CONUS. b) Percentage of area equipped for irrigation over the CONUS from the Global Map of Irrigation Areas (GMIA; Siebert et al., 2013).

2.3. Assessment of spatial patterns using auxiliary data

Figure 4 shows the spatial correlation between irrigation estimates from SM-DELTA (CCI Passive & FLUXCOM) (in green), SM-INVERSION (CCI Passive) (in blue), and NOAH-MP (Landsat) (in red) during the peak irrigation season (June to August) and the percentage of irrigated areas per pixel from GMIA (see Figure 3b) for the four main CONUS irrigation regions (see Figure 3a). The x-axis represents the percentage of irrigated area per pixel, while the y-axis represents the estimated irrigation volume per pixel. The Pearson correlation coefficient (R) is shown on each plot.

We can see that SM-DELTA (CCI Passive & FLUXCOM) and NOAH-MP (Landsat) correlate positively in all four regions. SM-DELTA (CCI Passive & FLUXCOM) reaches $R > 0.70$ in the semi-arid regions of the California Valley and Snake River Plain, and $R \geq 0.45$ in the wetter regions of the Great Plains and Mississippi Floodplain. Similarly, NOAH-MP (Landsat) maintains a strong correlation ($R \geq 0.70$) in the California Valley, Snake River Plain, and Great Plains, while reaching 0.55 in the Mississippi floodplain. In contrast, SM-INVERSION (CCI Passive) shows no significant correlation.

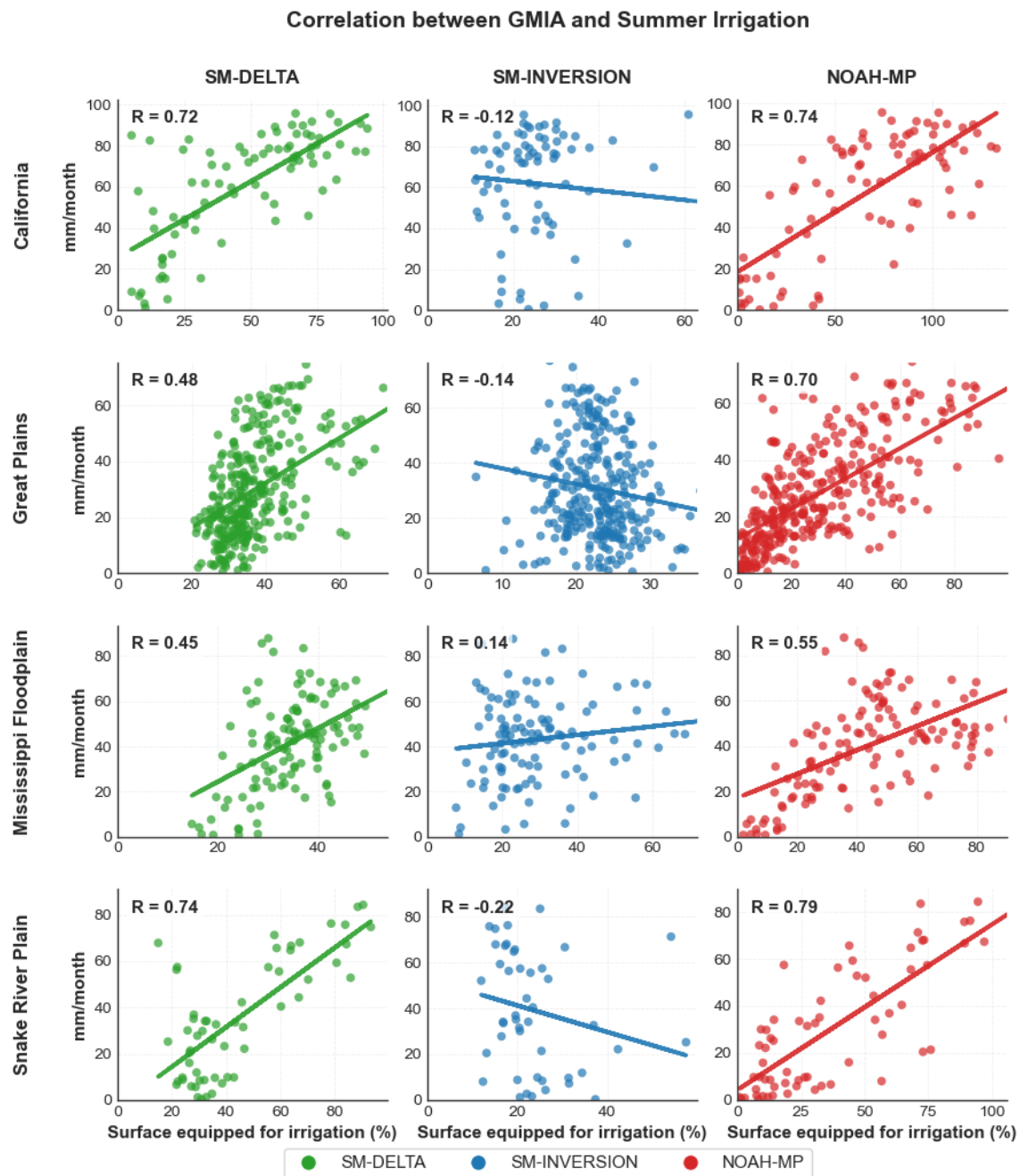


Figure 4: Correlation between surface equipped for irrigation and average irrigation over the period from June to August estimated with the three selected datasets over the four most irrigated regions of CONUS.

2.4. Intercomparison of temporal dynamics

Figure 5 presents the monthly irrigation estimates from SM-INVERSION (CCI Passive, blue), SM-DELTA (CCI Passive & FLUXCOM, green), and NOAA-MP (Landsat, red) for the four most irrigated regions of CONUS over the period 2003–2022. All values are spatially averaged over each region. The seasonal cycle is also shown, computed using only the common period across all three datasets (2010–2020).

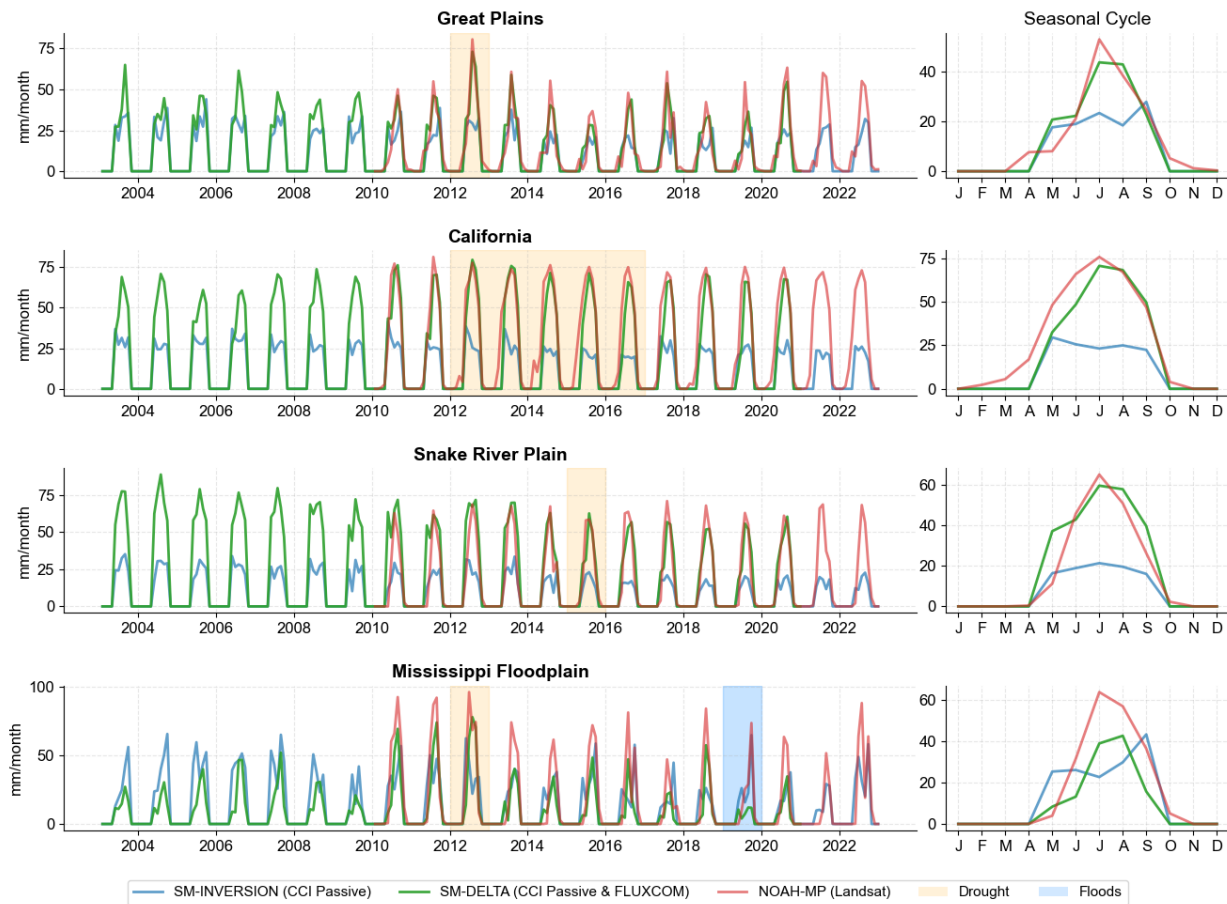


Figure 5: Left: Mean monthly irrigation estimates from SM-INVERSION (CCI Passive) in blue, SM-DELTA (CCI Passive & FLUXCOM) in green, and NOAA-MP (Landsat) in red for the four main irrigated regions of CONUS. Right: Seasonal cycle of the three datasets for each region.

A strong agreement appears between SM-DELTA (CCI Passive & FLUXCOM) and NOAA-MP (Landsat) in three regions (Great Plains, California Valley, and Snake River Plain). These two datasets show a similar seasonal pattern, with a pronounced irrigation peak in July and August, and exhibit strong interannual consistency. This similarity is particularly evident in the Great Plains, where both show marked year-to-year fluctuations — for example, a peak in July 2012 of 70 to 80 mm, and much lower irrigation (30 to 40 mm) in 2015. The agreement between SM-DELTA and NOAA-MP in three of the four regions is notable given their independent methodologies and input data, suggesting consistency in the representation of irrigation seasonality. SM-INVERSION (CCI Passive), on the other hand, provides a distinct seasonal pattern, with systematically lower irrigation estimates.

For the Mississippi Floodplain, the three datasets diverge significantly in both magnitude and temporal dynamics, with NOAH-MP showing a higher amount of irrigation than SM-DELTA and SM-INVERSION. This discrepancy is largely due to the sensitivity of NOAH-MP to the irrigation fraction data used in the algorithm, coupled with the fact that the Landsat-derived irrigation map it uses contains high irrigation fractions (>0.8) in this region (not shown).

Figure 5 shows the exceptionally dry years that occurred in each of the regions in yellow, as well as a particularly wet year in the Mississippi floodplain in 2019 that led to major flooding, in blue. Notably, 2012, a year of severe drought in the Great Plains, corresponds to the highest irrigation estimates from SM-DELTA (CCI PASSIVE & FLUXCOM) and NOAH-MP (Landsat) (>75 mm in July), reflecting a potential increase in irrigation demand in this region during that year. The reduction in irrigation requirements due to the heavy rains and flooding that occurred in 2019 in the Mississippi floodplain is reflected in SM-DELTA (CCI PASSIVE & FLUXCOM), which shows a very low peak in irrigation (less than 15 mm/month) in July 2019. However, the severe drought of 2015 in California and the Snake River Plain is not reflected in the estimates.

3. Ebro Basin

3.1. Evaluation with in situ irrigation data

The six datasets obtained with SM-DELTA and the five obtained with SM-INVERSION were validated using in situ data from four irrigation districts in the eastern part of the Ebro Basin (Figure 6) for the period 2007–2020. Given the mismatch in scale between the resolution of the dataset (pixel size of 0.25°) and the boundaries of the irrigation districts, the in situ data were aggregated into a single virtual district to enable a more consistent comparison. Only pixels with at least 25% of their surface area covered by the irrigation district were kept in the analysis.

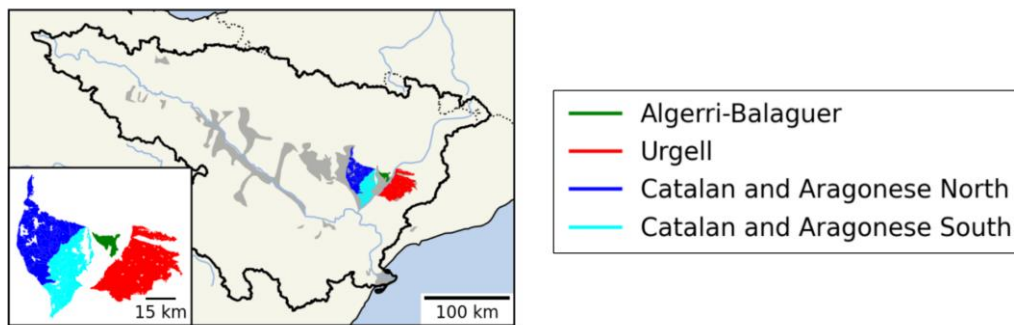


Figure 6: The four irrigation districts in the Ebro Basin for which in situ data are available and have been used to validate the datasets obtained with the SM-DELTA and SM-INVERSION-derived datasets.

Table 3 presents the RMSD, bias, and R values obtained from the six SM-DELTA datasets and the five SM-INVERSION datasets. Note that the metrics were calculated only during the irrigation periods (April to October). All datasets show an underestimation of irrigation. The six SM-DELTA datasets show similar values for RMSD, bias, and R. The SM-INVERSION datasets show more pronounced underestimations than the SM-DELTA datasets, along with lower Pearson R values, except for SM-INVERSION (CCI PASSIVE), which shows metrics of the same order of magnitude as those obtained with the SM-DELTA datasets.

Table 3: Metrics values (RMSD, bias, Pearson) obtained over the Ebro irrigation districts for the period 2007–2020 for the six datasets obtained with the SM-DELTA method and the five datasets obtained with the SM-INVERSION method.

Method	Dataset	RMSD (mm/month)	Bias (mm/month)	Pearson R (-)
SM-DELTA	CCI Combined & FLUXCOM	29,98	-22,23	0,6
	CCI Passive & FLUXCOM	29,04	-17,15	0,63
	CCI Active & FLUXCOM	29,41	-20,65	0,54
	CCI Combined & SSEBOP	27,28	-17,2	0,6
	CCI Passive & SSEBOP	29,22	-22,28	0,69
	CCI Active & SSEBOP	28,83	-20,7	0,62

SM-INVERSION	CCI Combined	41,3	-34,11	0,37
	CCI Passive	30	-22,98	0,63
	ASCAT	47,25	-39,8	0,12
	SMOS	29	-35,38	0,06
	SMAP	46,02	-36,58	0,1

Figure 9 presents the monthly in situ irrigation (shaded grey area) along with irrigation estimates from SM-DELTA (CCI Active & FLUXCOM) and SM-INVERSION (ASCAT) (Figure 9a), SM-DELTA (CCI Combined & FLUXCOM) and SM-INVERSION (CCI Combined) (Figure 9b), and SM-DELTA (CCI Passive & FLUXCOM) and SM-INVERSION (CCI Passive) (Figure. 9c). The corresponding metric values are shown in the legend. A similar figure, but with the SM-DELTA datasets using SSEBOP ET instead of those using FLUXCOM ET is presented in Figure A1 (Appendix). A key observation is a noticeable temporal consistency across the datasets.

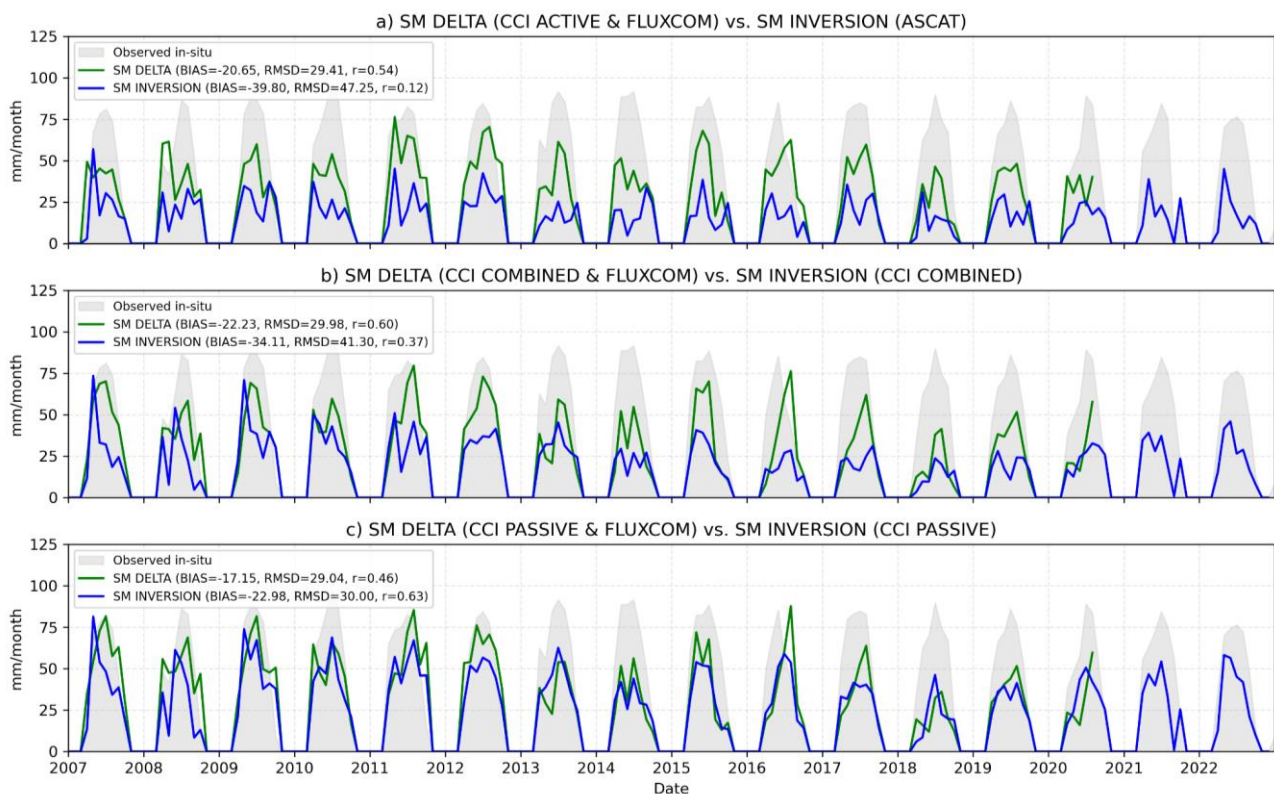


Figure 9: Average monthly irrigation over the irrigation districts of the eastern Ebro from the three SM-DELTA datasets using FLUXCOM ET (green lines), the three SM-INVERSION datasets (CCI Combined, CCI PASSIVE, ASCAT), along with the in situ data (grey shaded area).

3.2. Intercomparison of spatial patterns

Figure 10 presents the mean summer season (May to August) irrigation map for the common period across the six datasets (2003-2020), along with the GMIA map showing the percentage of area equipped for irrigation, for the Ebro Basin.

It can be noted that i) irrigation estimates from SM-INVERSION tend to be slightly lower, consistent with the findings from Figure 9 and Table 3, ii) the three SM-DELTA datasets show higher irrigation levels in the eastern part of the district, which corresponds to pixels with more irrigation equipment according to GMIA, and iii) in contrast, the three SM-INVERSION datasets exhibit a more homogeneous pattern, with particularly high irrigation in the Ebro Delta (the three pixels in the southeast) for CCI Passive, an area known for intensive irrigation.

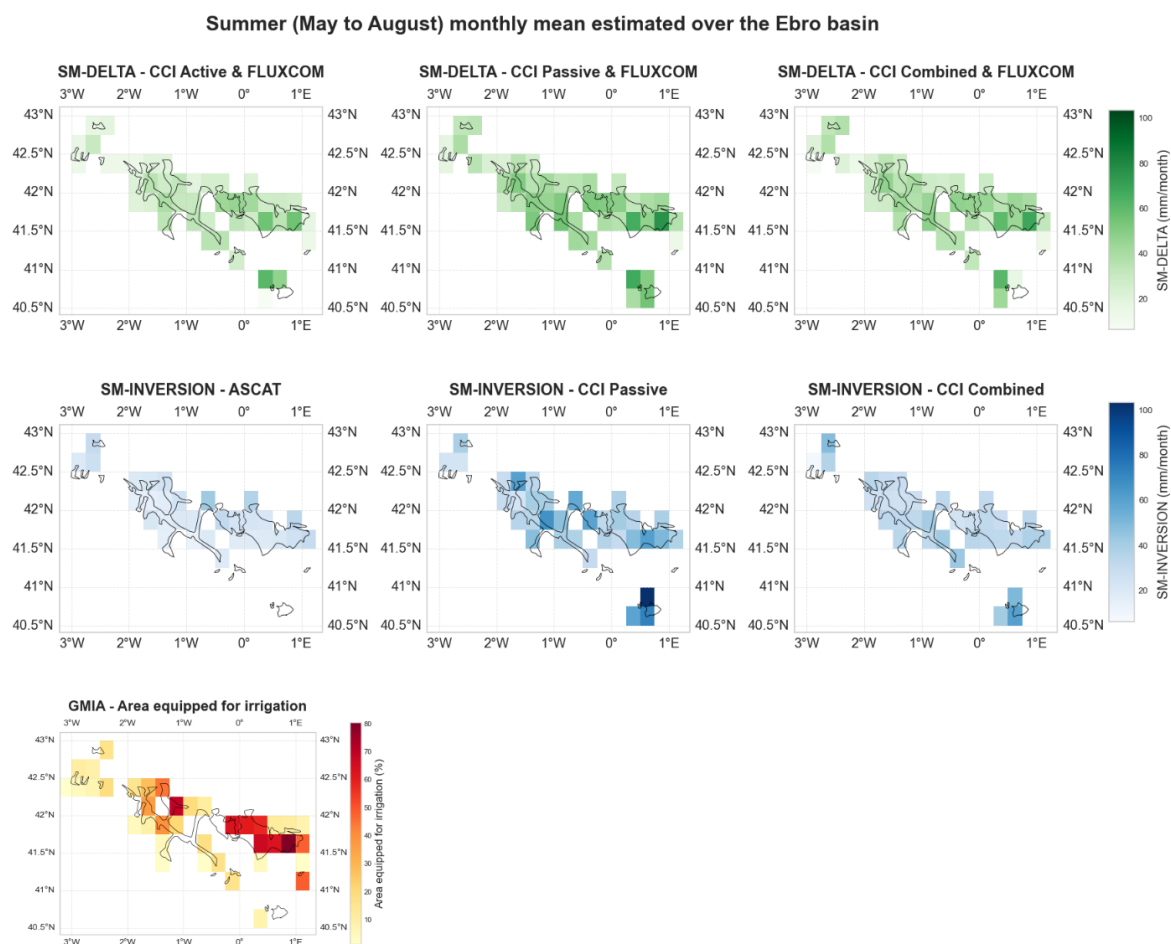


Figure 10: Summer season irrigation maps (May to August) for the period 2003-2020 for three datasets obtained with SM-DELTA (in green) and three datasets obtained with SM-INVERSION (in blue). The map of the percentage of area equipped for irrigation is also shown (third line).

3.3. Assessment of spatial patterns using auxiliary data

Figure 11 illustrates the spatial correlation between irrigation volume (x-axis) during the summer irrigation season (May to August) and the percentage of area equipped for irrigation (y-axis) from GMIA for the three SM-DELTA datasets (in green) and the three SM-INVERSION datasets. (in blue).

The SM-DELTA datasets show a positive correlation ($R \geq 0.59$), largely due to the higher irrigation quantities observed in the eastern part of the district, matching the pixels with the highest percentage of area equipped for irrigation. In contrast, the SM-INVERSION datasets show no correlation.

Correlation between GMIA and summer irrigation (May to August) over the Ebro basin

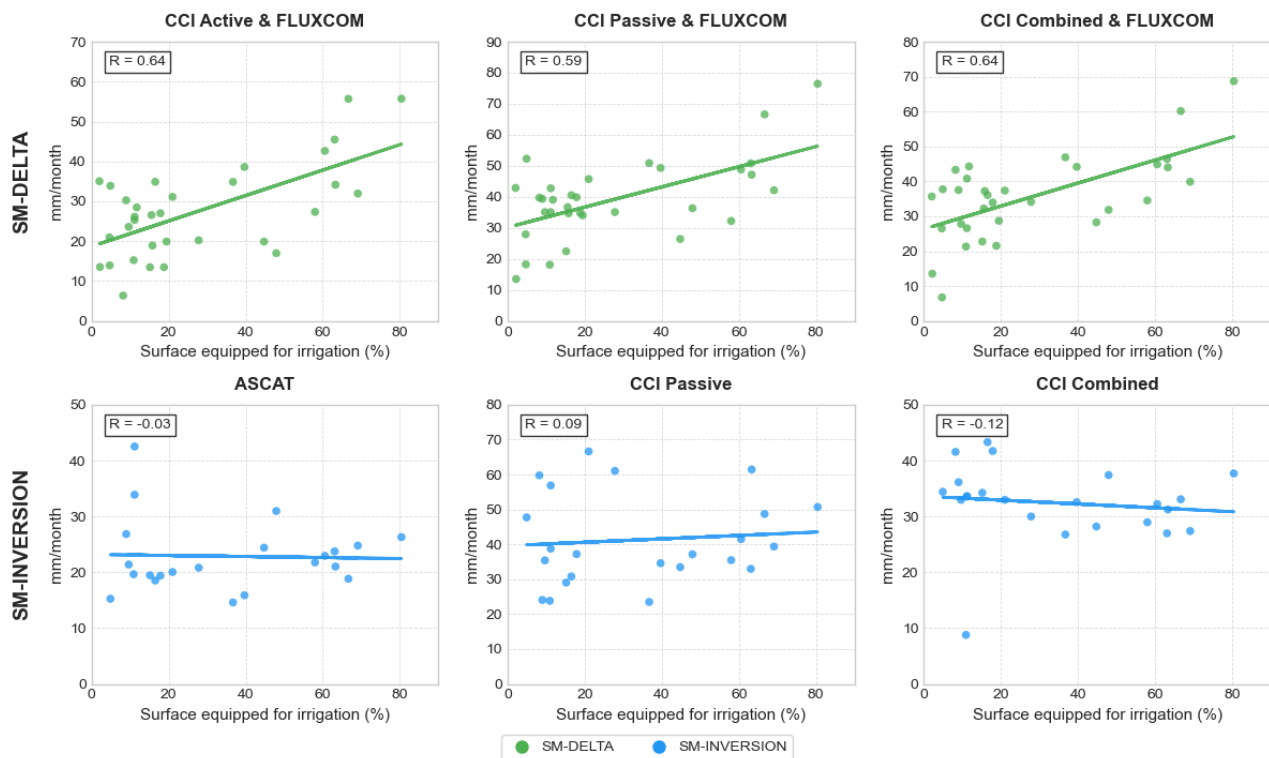


Figure 11: Correlation between surface equipped for irrigation and average monthly irrigation over the period from May to August estimated with three selected datasets obtained with SM-DELTA (in green) and three obtained with SM-INVERSION (in blue) over the Ebro Basin.

3.4. Intercomparison of temporal dynamics

Figure 12 presents the monthly irrigation estimates spatially averaged over the entire Ebro Basin for different datasets: SM-INVERSION (CCI Combined) and SM-DELTA (CCI Combined & FLUXCOM) (Figure 12a), SM-INVERSION (CCI Passive) and SM-DELTA (CCI Combined & FLUXCOM) (Figure 12b), and SM-INVERSION (ASCAT) and SM-DELTA (CCI Active & FLUXCOM) (Figure 12). The right panels show the corresponding seasonal cycles with standard deviations, considering only the pixels in common between all the datasets and the period in common (2007-2020).

A key observation is the strong similarity in temporal dynamics and magnitudes for SM-INVERSION (CCI Passive), SM-DELTA (CCI Passive & FLUXCOM), SM-INVERSION (CCI Combined), and SM-DELTA (CCI Combined & FLUXCOM). All four datasets highlight wetter irrigation years between 2004 and 2013, a drier year in 2014, and lower irrigation levels in 2018 and 2019. It can be seen from the seasonal cycle plots that the peak in irrigation occurs in May for the SM-INVERSION datasets, while it occurs in July-August for the SM-DELTA datasets. On the other hand, SM-DELTA (CCI Active & FLUXCOM) and SM-INVERSION (ASCAT) present significantly different dynamics, with systematically lower irrigation estimates, particularly for SM-INVERSION (ASCAT).

Monthly irrigation estimates over the Ebro Basin

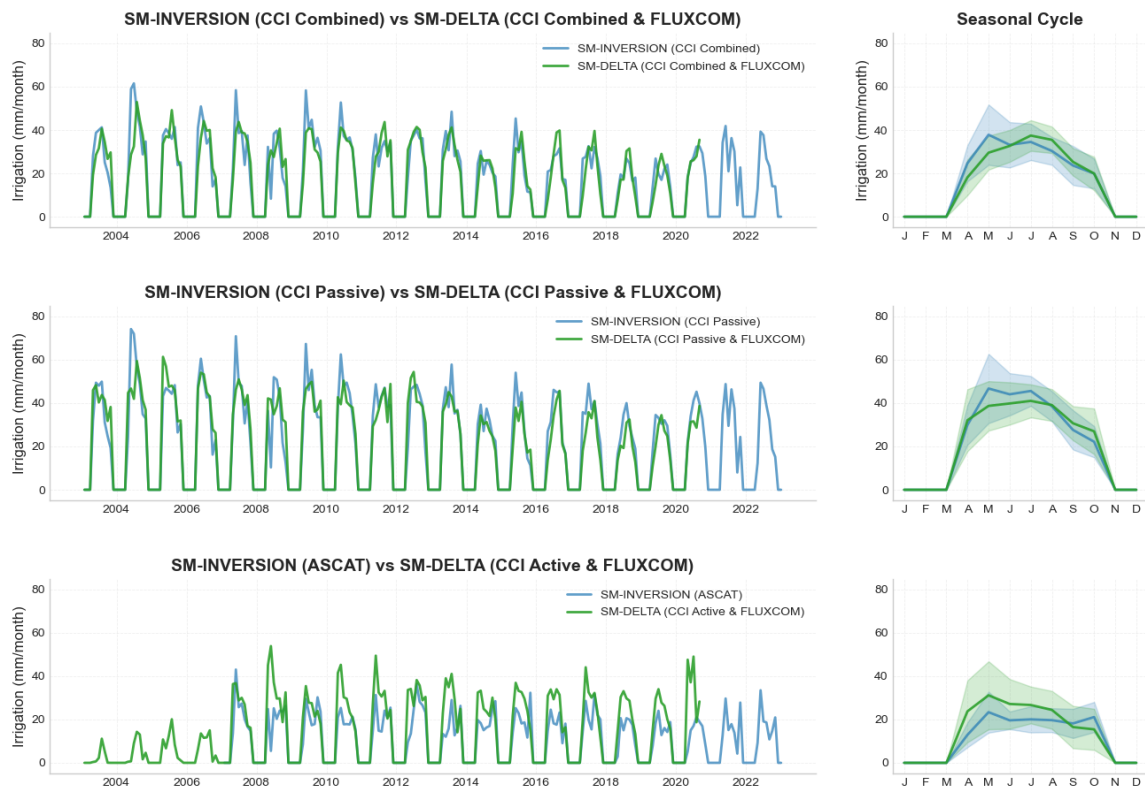


Figure 12: Monthly mean irrigation estimates from three irrigation datasets obtained with SM-INVERSION (in blue) and three datasets obtained with SM-DELTA (in green). The right panel shows the corresponding seasonal cycle with standard deviation along with the seasonal cycle of the averaged in situ data.

4. Murray-Darling Basin

4.1. Evaluation with in situ irrigation data

Six datasets obtained with SM-DELTA, five obtained with SM-INVERSION, and one obtained with NOAH-MP were validated using in situ data from four irrigation districts located in the southeastern part of the Murray-Darling Basin (Figure 12). The validation period spans 2009-2010 to 2020, with RMSD, bias, and R computed as performance metrics. Note that the months outside of the irrigation season, from May to September, were masked. Only pixels with centroids located within the district were kept in the analysis.

The validation method used here for the Murray-Darling Basin irrigation districts differs from that used in the D4 PVSAR (sections 2.1 and 3.4), leading to differences in the reported metrics. Here, the observed irrigation volume is divided by the total district area rather than the area of effectively irrigated fields, resulting in a lower observed irrigation depth. By doing so, in situ irrigation becomes more consistent with the satellite-derived estimates, as satellite pixels capture both irrigated and non-irrigated fields.

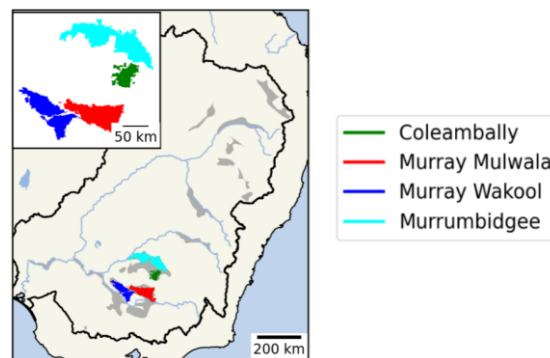


Figure 13: The four irrigation districts in the Murray-Darling Basin for which in situ data are available and have been used to validate the datasets obtained with the SM-DELTA, SM-INVERSION, and NOAH-MP methods.

Table 4 presents RMSD, bias, and Pearson R for the six SM-DELTA datasets, the five SM-INVERSION datasets, and NOAH-MP (Landsat) across the four irrigation districts. Figures 13 to 16 illustrate the corresponding monthly irrigation estimates, while additional results using FLUXCOM-based SM-DELTA datasets are provided in the Appendix (Figures A2–A5).

Performance varies across districts, with no single dataset consistently outperforming the others. SM-DELTA datasets using SSEBOP ET tend to show better correspondence with reference estimates in Murrumbidgee and Coleambally, where correlation values are generally higher and both RMSD and bias are moderate. In Murray Mulwala and Murray Wakool, the results are more mixed, with lower correlations and greater variability across datasets.

The performance of SM-INVERSION datasets also depends on the district and the specific product. Some, such as CCI Passive, produce results comparable to those of SM-DELTA in certain cases, while others like ASCAT, tend to show more frequent overestimations and lower correlation. SMAP performs relatively well

in Murray Wakool and Coleambally, although its shorter period of availability limits comparisons with other datasets.

NOAH-MP (Landsat) shows contrasting performance across regions. It performs relatively well in Murray Mulwala and Coleambally, while in other districts, RMSD and bias are generally higher than for most SM-based datasets.

Table 4: Metrics values (RMSD, Bias, Pearson) obtained on the four irrigation districts in the Murray-Darling Basin for the six datasets obtained with the SM-DELTA method, the five datasets obtained with the SM-INVERSION method, and the NOAH-MP (Landsat) dataset.

Method	Dataset	Murray Mulwala			Murray Wakool		
		RMSD (mm/month)	Bias (mm/month)	Pearson R (-)	RMSD (mm/month)	Bias (mm/month)	Pearson R (-)
SM-DELTA	CCI COMBINED & FLUXCOM	13,19	4,45	0,28	14,30	10,32	0,16
	CCI PASSIVE & FLUXCOM	14,89	7,28	0,24	16,19	13,04	0,22
	CCI ACTIVE & FLUXCOM	12,95	-3,80	0,22	11,33	5,71	0,12
	CCI COMBINED & SSEBOP	14,80	0,51	0,06	12,54	5,93	0,18
	CCI PASSIVE & SSEBOP	16,31	3,34	0,04	14,21	8,65	0,23
	CCI ACTIVE & SSEBOP	15,64	-7,74	-0,01	10,24	1,31	0,16
SM-INVERSION	CCI COMBINED	13,92	4,00	0,00	12,41	9,21	0,15
	CCI PASSIVE	13,38	6,19	0,32	16,05	13,91	0,35
	ASCAT	18,59	12,29	0,20	14,91	11,39	0,32
	SMOS	16,43	8,55	0,11	19,12	15,62	0,36
	SMAP	11,65	4,91	0,18	12,81	10,08	0,35
NOAH-MP	Landsat	14,92	9,01	0,47	16,13	14,19	0,33
Method	Dataset	Murrumbidgee			Coleambally		
		RMSD (mm/month)	Bias (mm/month)	Pearson R (-)	RMSD (mm/month)	Bias (mm/month)	Pearson R (-)
SM-DELTA	CCI COMBINED & FLUXCOM	13,07	6,85	0,15	18,82	3,73	0,44
	CCI PASSIVE & FLUXCOM	15,20	10,31	0,29	20,91	6,59	0,39

	CCI ACTIVE & FLUXCOM	13,15	1,93	-0,03	19,60	4,75	0,43
	CCI COMBINED & SSEBOP	11,72	4,38	0,38	16,34	0,50	0,54
	CCI PASSIVE & SSEBOP	15,83	7,83	0,41	19,79	2,36	0,45
	CCI ACTIVE & SSEBOP	10,83	-0,55	0,23	17,95	8,98	0,57
SM-INVERSION	CCI COMBINED	11,72	4,38	0,38	21,44	3,99	-0,11
	CCI PASSIVE	15,83	7,83	0,41	22,20	0,28	0,02
	ASCAT	22,85	13,09	-0,12	27,22	11,81	0,00
	SMOS	18,23	13,57	0,10	21,37	7,14	0,20
	SMAP	9,64	4,15	0,38	15,82	1,80	0,12
NOAH-MP	Landsat	7,59	4,87	0,66	28,80	17,68	0,41

Murray_Mulwala (Area: 1480.0 km²)

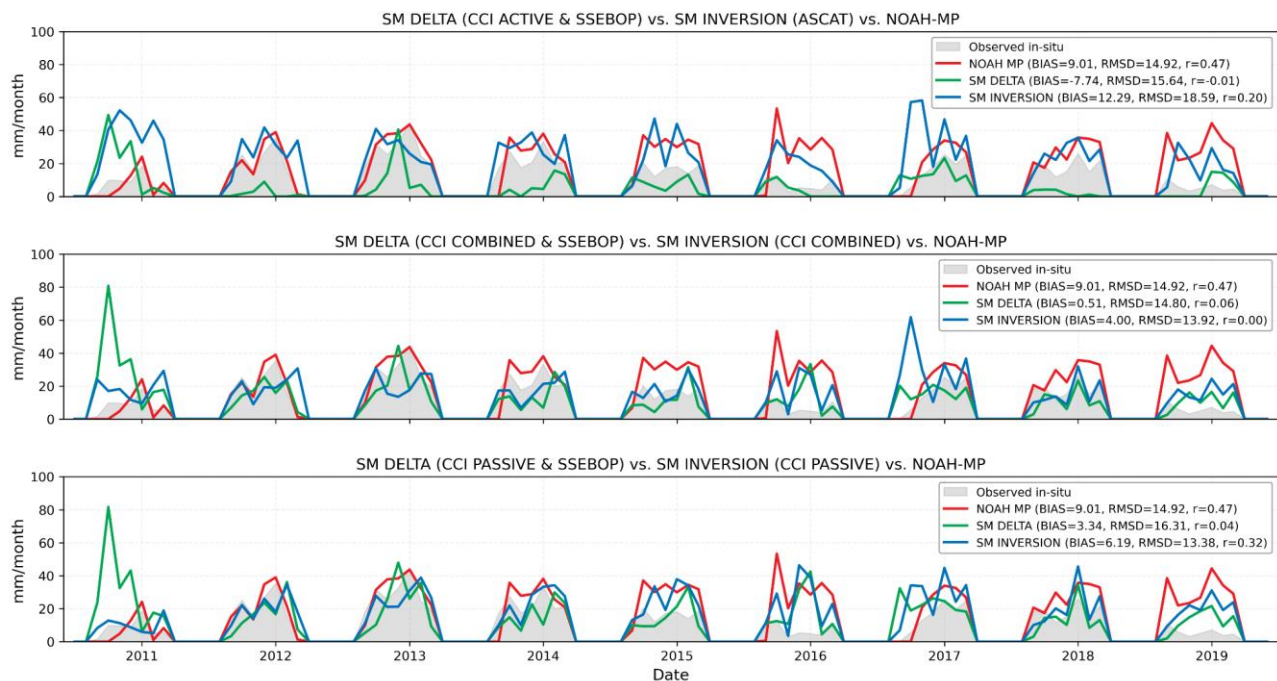


Figure 13: Average monthly irrigation over the Murray Mulwala irrigation districts from three SM-DELTA datasets using SSEBOP ET (green lines), three SM-INVERSION datasets (CCI Combined, CCI Passive, ASCAT), with the in situ data (grey shaded area).

Murray_Wakool (Area: 1275.0 km²)



Figure 14: Same as Figure 13 but for the Murray Wakool irrigation district.

Murrumbidgee (Area: 1600.0 km²)

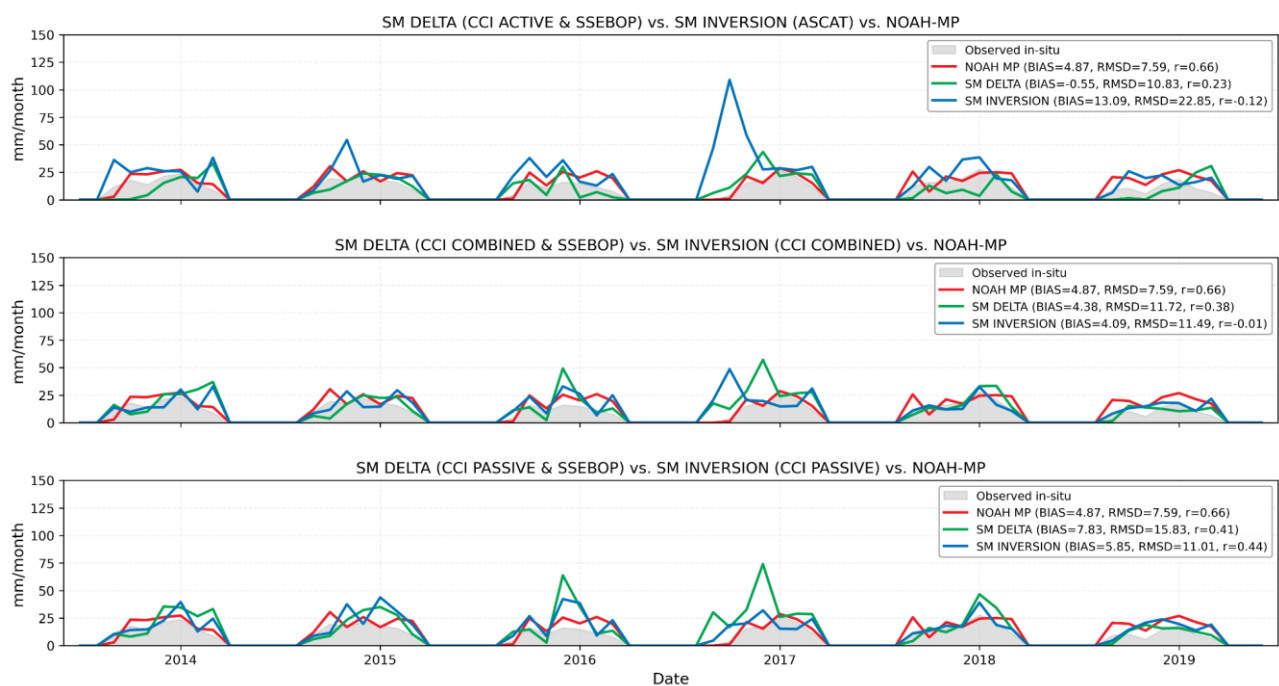


Figure 15: Same as Figures 13 and 14 but for the Murrumbidgee irrigation district.

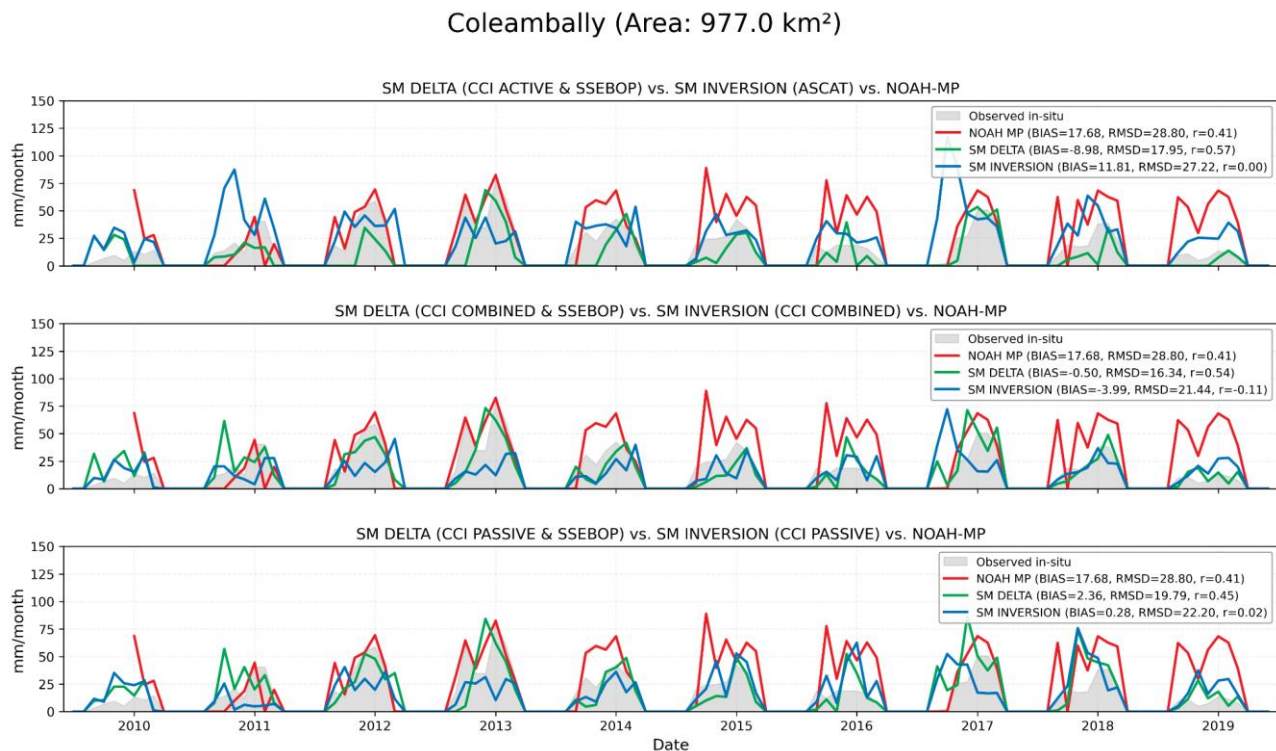


Figure 16: Same as Figures 13, 14, and 15 but for the Coleambally irrigation district.

4.2. Intercomparison of spatial patterns

Figure 17 shows mean annual irrigation maps over the common period (2010–2020) for the six datasets obtained with SM-DELTA (in green), the five datasets obtained with SM-INVERSION (in blue), and the NOAH-MP (Landsat) dataset (in red). The map of the percentage of area equipped for irrigation is also shown (bottom right). The most irrigated areas are shown in thin black lines.

Both SM-DELTA (CCI Active & FLUXCOM) and SM-DELTA (CCI Active & SSEBOP) show lower irrigation values compared to other SM-DELTA datasets. SM-DELTA (CCI Combined & FLUXCOM) and SM-DELTA (CCI Passive & FLUXCOM) show higher irrigation amounts than SM-DELTA (CCI Combined & SSEBOP) and SM-DELTA (CCI Passive & SSEBOP), particularly in the southern regions where the density of area equipped for irrigation is the highest.

Among the SM-INVERSION datasets, ASCAT exhibits significantly higher irrigation values than the others.

The NOAH-MP dataset shows irrigation concentrated primarily in the south along the Murray River, with additional irrigated areas in the northeast.

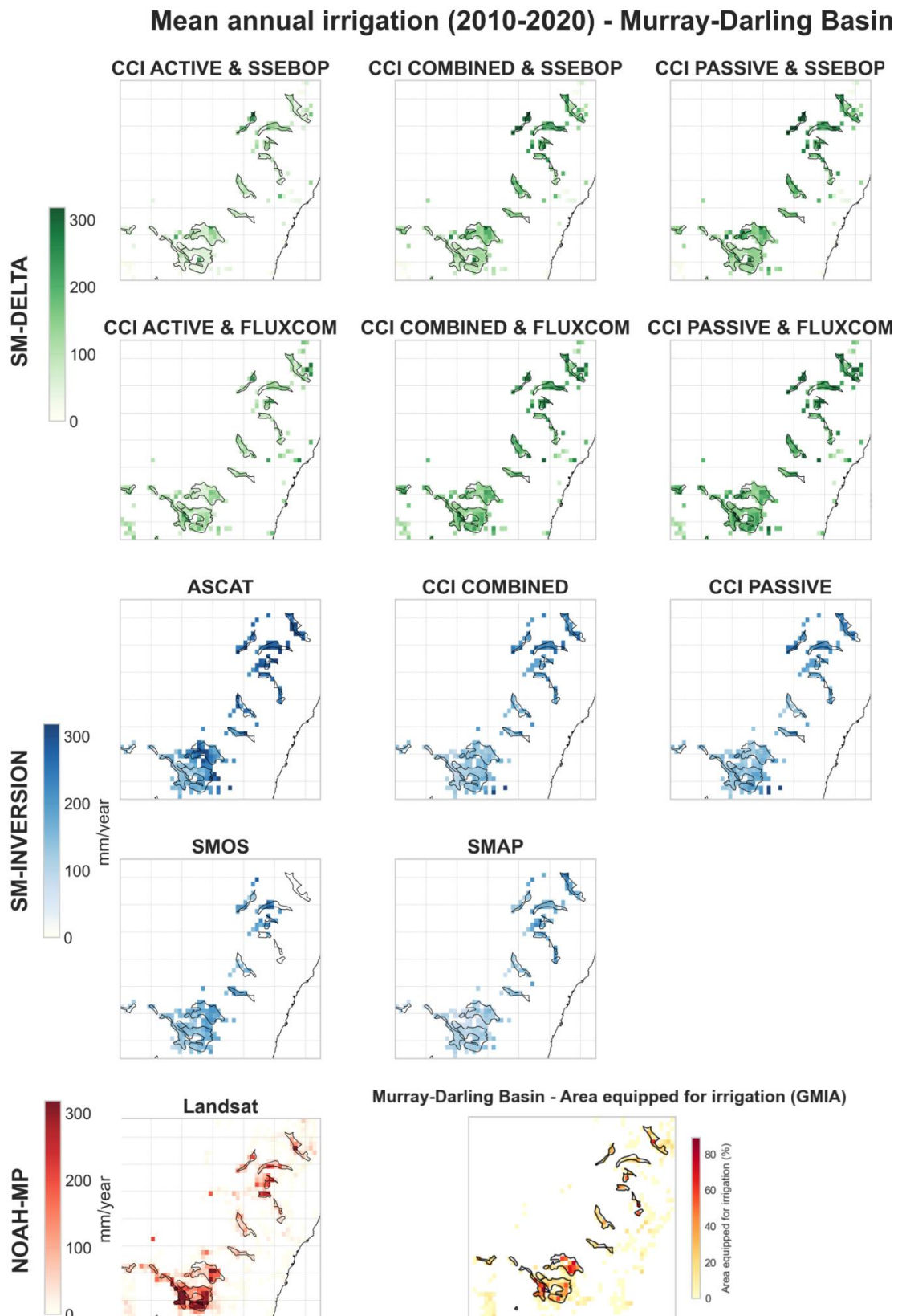


Figure 17: Irrigation maps of mean annual irrigation for the period 2010-2020 for six datasets obtained with SM-DELTA (in green), five datasets obtained with SM-INVERSION (in blue), and the NOAH-MP (Landsat) dataset (in red). The map of the percentage of area equipped for irrigation is also shown (bottom right).

4.3. Assessment of spatial patterns using auxiliary data

Figure 18 presents the correlation between the percentage of area equipped for irrigation and the mean monthly irrigation estimates from November to March over the common period (2010–2020). The analysis includes six SM-DELTA datasets (green), five SM-INVERSION datasets (blue), and NOAH-MP (Landsat).

The SM-INVERSION datasets show no correlation with equipped irrigation (mean $R = -0.04$), as for the three SM-DELTA datasets including SSEBOP ET (mean $R = 0.06$). In contrast, the SM-DELTA datasets using FLUXCOM ET show a weak positive correlation, with Pearson R values of 0.32 for CCI Active & FLUXCOM, 0.15 for CCI Passive & FLUXCOM, and 0.16 for CCI Combined & FLUXCOM. NOAH-MP (Landsat) exhibits the strongest correlation, with $R = 0.62$.

Correlation between surface equipped for irrigation and irrigation datasets - Murray-Darling Basin

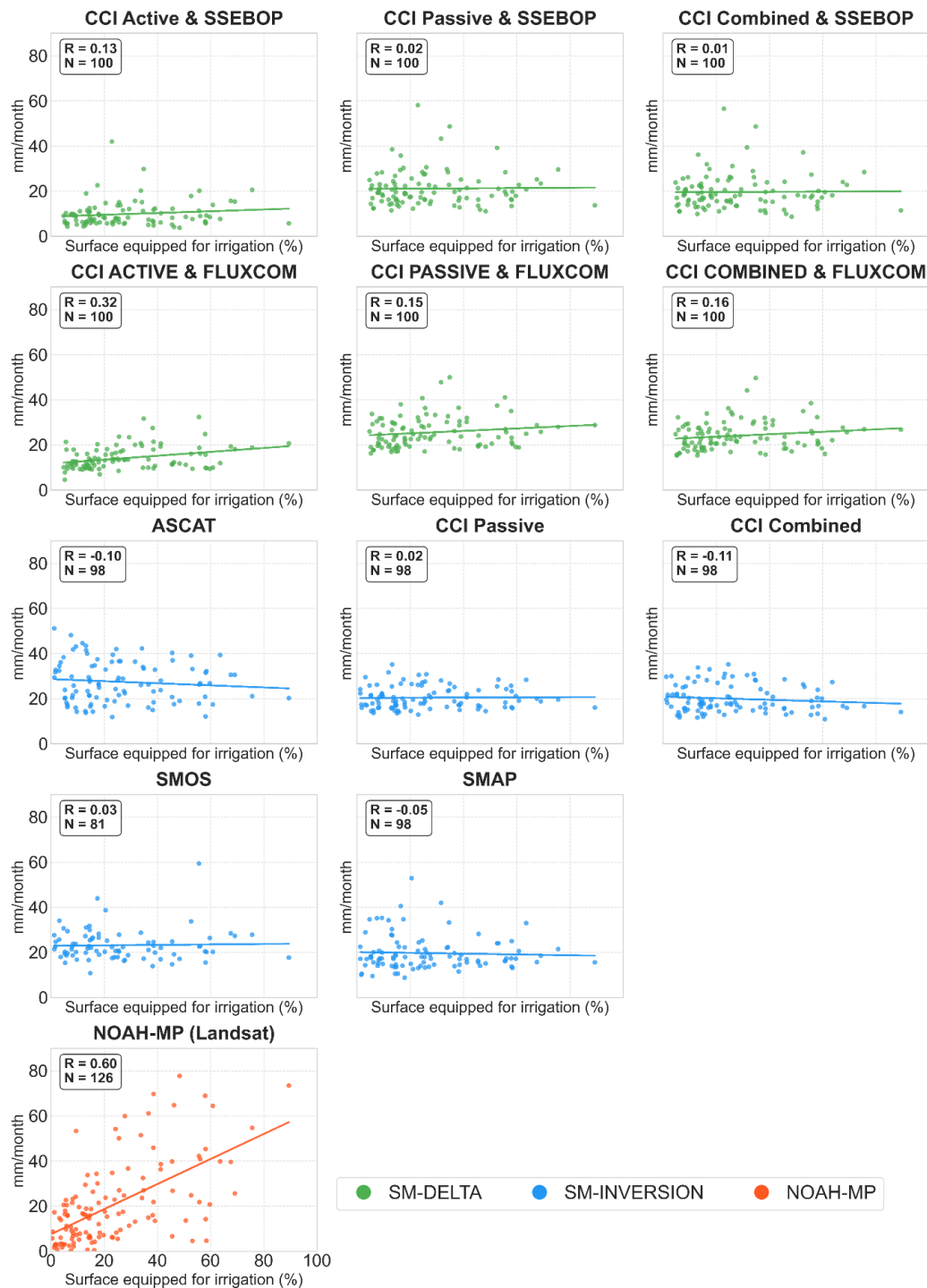


Figure 18: Correlation between surface equipped for irrigation and average monthly irrigation over the period from November to March estimated with the six datasets obtained with SM-DELTA (in green), the five obtained with SM-INVERSION (in blue), and NOAH-MP (Landsat) over the Murray-Darling Basin.

4.4. Intercomparison of temporal dynamics

Figure 19 shows monthly irrigation estimates for three SM-INVERSION datasets (CCI Passive, CCI Combined, CCI Active), six SM-DELTA datasets (CCI Passive & FLUXCOM, CCI Combined & FLUXCOM, CCI Active & FLUXCOM, CCI Passive & SSEBOP, CCI Combined & SSEBOP, CCI Active & SSEBOP), and the NOAH-MP (Landsat) dataset. The corresponding seasonal cycles are displayed on the right, computed using only the common period (2010-2020). These estimates are spatial averages over the entire basin.

SM-INVERSION (CCI Passive and CCI Combined) closely match the temporal dynamics of SM-DELTA datasets using the same CCI products, while SM-INVERSION (ASCAT) and SM-DELTA (CCI Active) show clear discrepancies. Seasonal cycles are consistent for most of the datasets, with higher irrigation between November and February, except for the three SM-DELTA datasets including FLUXCOM ET, which show high values in September. NOAH-MP (Landsat) shows lower irrigation levels than the other datasets, likely due to irrigation being concentrated in specific pixels in the southern part of the basin.

Estimates of monthly mean irrigation over the Murray-Darling basin

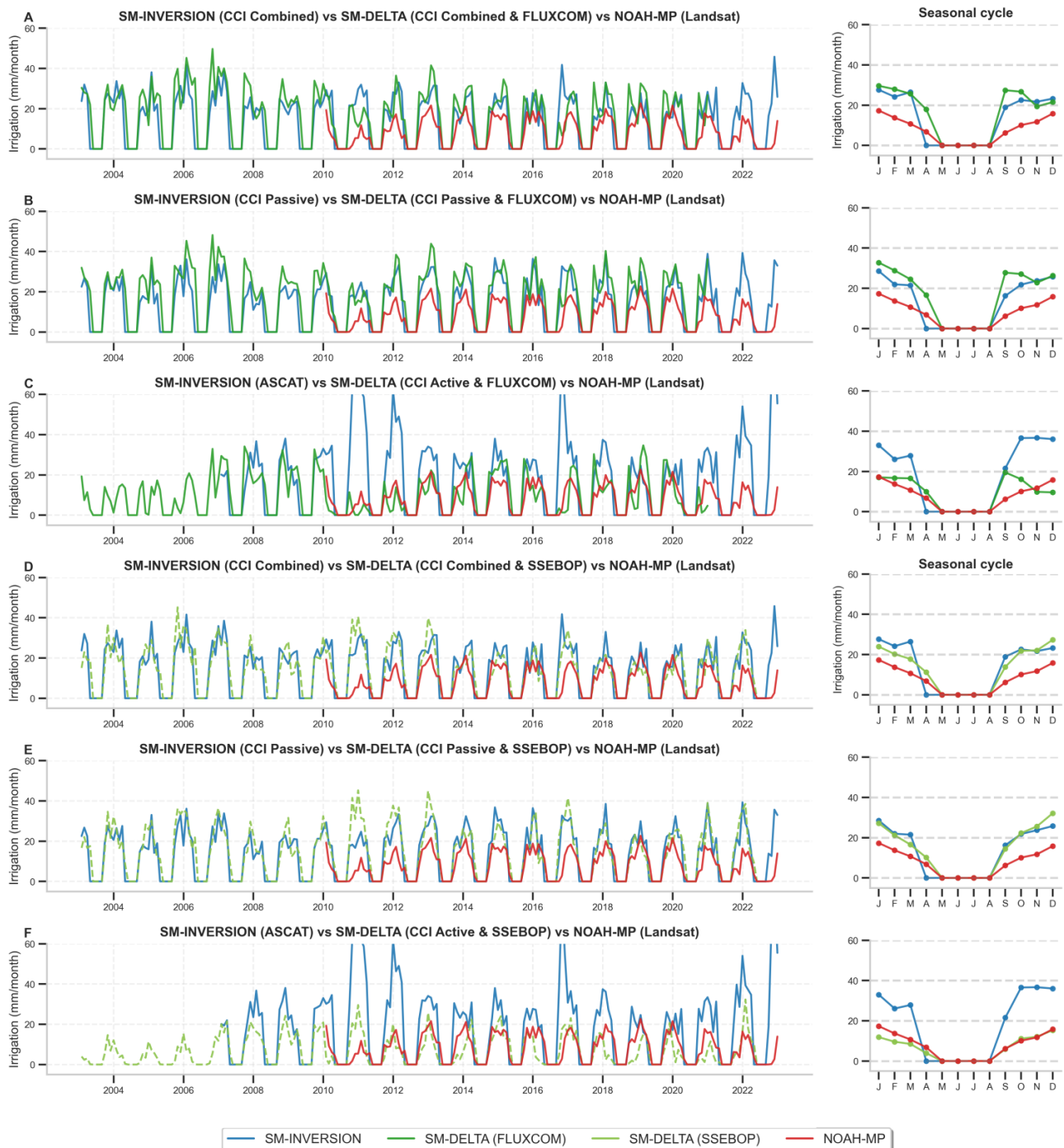


Figure 19: Monthly mean irrigation estimates from three irrigation datasets obtained with SM-INVERSION (in blue), six datasets obtained with SM-DELTA (FLUXCOM in continuous green line and SSEBOP in dotted green line), and the NOAA-MP (Landsat) dataset (in red). The right panel shows the corresponding seasonal cycle along with the seasonal cycle of the averaged in situ data.

5. India

This section examines three datasets produced using the SM-DELTA method (CCI Combined & FLUXCOM, CCI Passive & FLUXCOM, and CCI Active & FLUXCOM) and five datasets obtained with the SM-INVERSION method (CCI Combined, CCI Passive, ASCAT, SMOS, SMAP). It is important to note that a temporal mask has been applied to the datasets, excluding months from July to October. This exclusion ensures consistency across datasets, as SM-INVERSION used these months for model parameter calibration.

5.1. Intercomparison of spatial patterns

Figure 20 presents the average annual irrigation map (excluding July to October) of India derived from three SM-DELTA datasets (green) and five SM-INVERSION datasets (blue). The last row of Figure 20 shows the Global Map of Irrigated Areas (GMIA), highlighting the Gangetic Plain in the north as the most irrigated region. SM-DELTA datasets using SSEBOP ET data were excluded due to excessively high irrigation estimates relative to precipitation and potential evapotranspiration (see Section 3.5 in D4 PVSAR for details).

The SM-INVERSION datasets estimate significantly higher irrigation levels than the SM-DELTA datasets (color bar scales reach 700 mm/year and 500 mm/year, respectively). Among the SM-INVERSION datasets, all except CCI Combined simulate higher irrigation levels in northern and eastern India, exceeding 700 mm/year. However, despite being highly equipped for irrigation, the northwestern part of the Gangetic plain shows lower irrigation estimates in these datasets. Conversely, the SM-DELTA datasets estimate lower irrigation levels, with SM-DELTA (CCI Active & FLUXCOM) showing the lowest values. In the northwest, SM-DELTA datasets estimates reach approximately 500 mm/year. Other densely irrigated regions, such as those near Bangladesh and along the eastern coast, also show relatively high irrigation estimates, particularly in the SM-DELTA (CCI Active & FLUXCOM) dataset.

Mean yearly irrigation in India

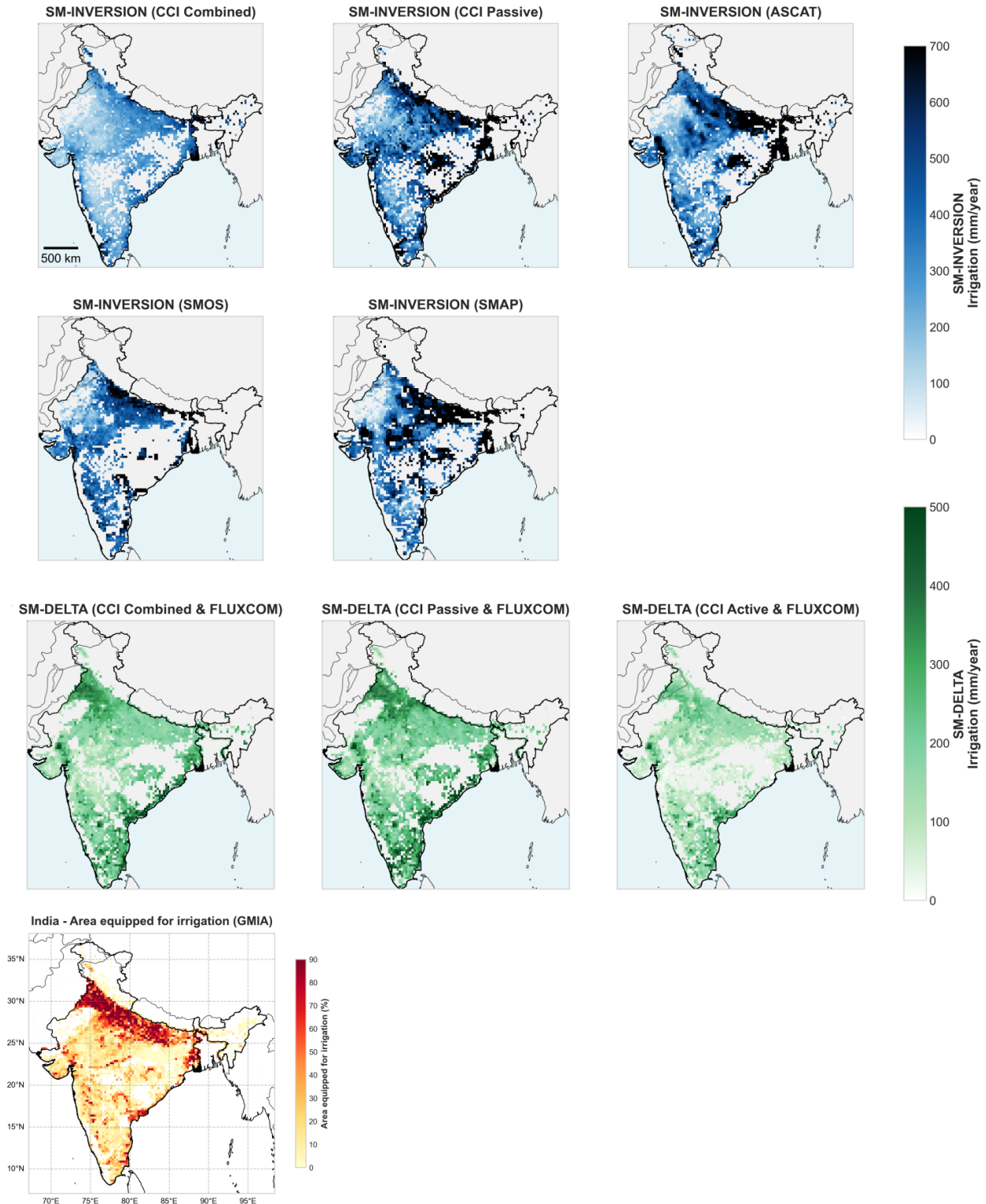


Figure 20: Irrigation maps of mean annual irrigation for three datasets obtained with SM-DELTA (in green) and five datasets obtained with SM-INVERSION (in blue). The map of the percentage of area equipped for irrigation is also shown (bottom line).

5.2. Assessment of spatial patterns using auxiliary data

The correlation between the area equipped for irrigation and simulated irrigation during the Rabi season (the most irrigated season, from November to April) over the Ganges Valley (the most irrigated region) is presented in Figure 21 for the five SM-INVERSION datasets and the three SM-DELTA datasets. SM-INVERSION datasets do not exhibit a significant correlation, with an average R-value of -0.12. The SM-DELTA datasets show a moderate correlation, with an average R-value of 0.40.

Correlation between GMIA and Mean Rabi (Nov. - April) Season Irrigation - India

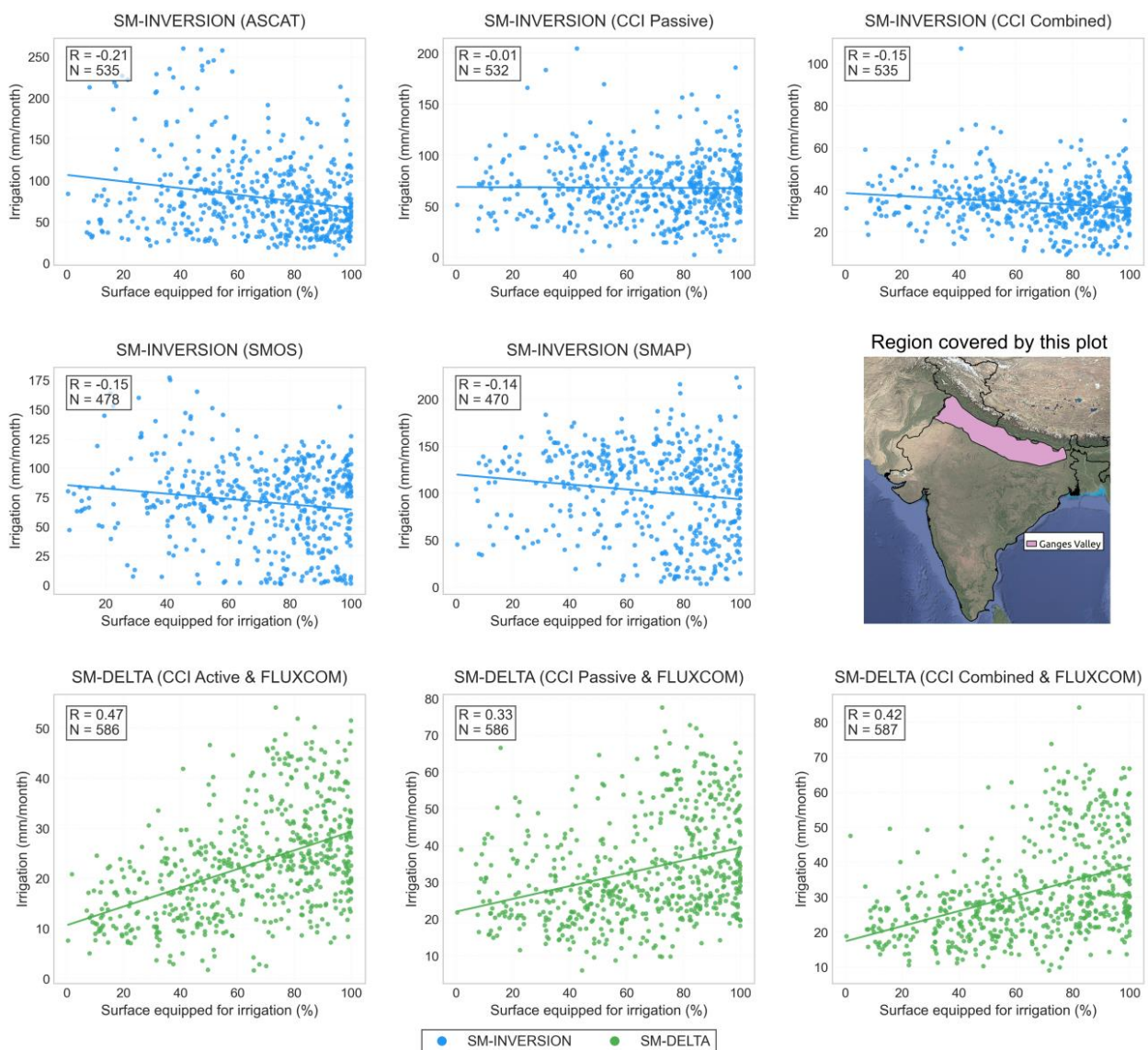


Figure 21: Correlation between surface equipped for irrigation and average monthly irrigation over the period from November to April estimated with the five datasets obtained with SM-INVERSION (in blue), and the three datasets obtained with SM-DELTA (in green) over the Ganges valley. A map of India with the Ganges Valley is also shown.

5.3. Intercomparison of temporal dynamics

Figure 22 presents monthly mean irrigation estimates over the Ganges Valley, derived from five SM-INVERSION datasets (blue) and three SM-DELTA datasets (green). The SM-INVERSION datasets estimate significantly higher irrigation levels than the SM-DELTA datasets, particularly from November to January, when they consistently show the highest values. In contrast, SM-DELTA datasets reach their peak irrigation estimates in March. For comparison, Kragh et al. (2023), who simulated irrigation over the Ganges Valley using a hydrological model combined with high-resolution (1 km) ET data, obtained irrigation values ranging from 10 to 50 mm/month during the Rabi season (November to April), with a peak of 40-50 mm/month in March, and from 10 to 30 mm/month for the rest of the year.

Estimates of monthly mean irrigation over the Indo-Gangetic plain

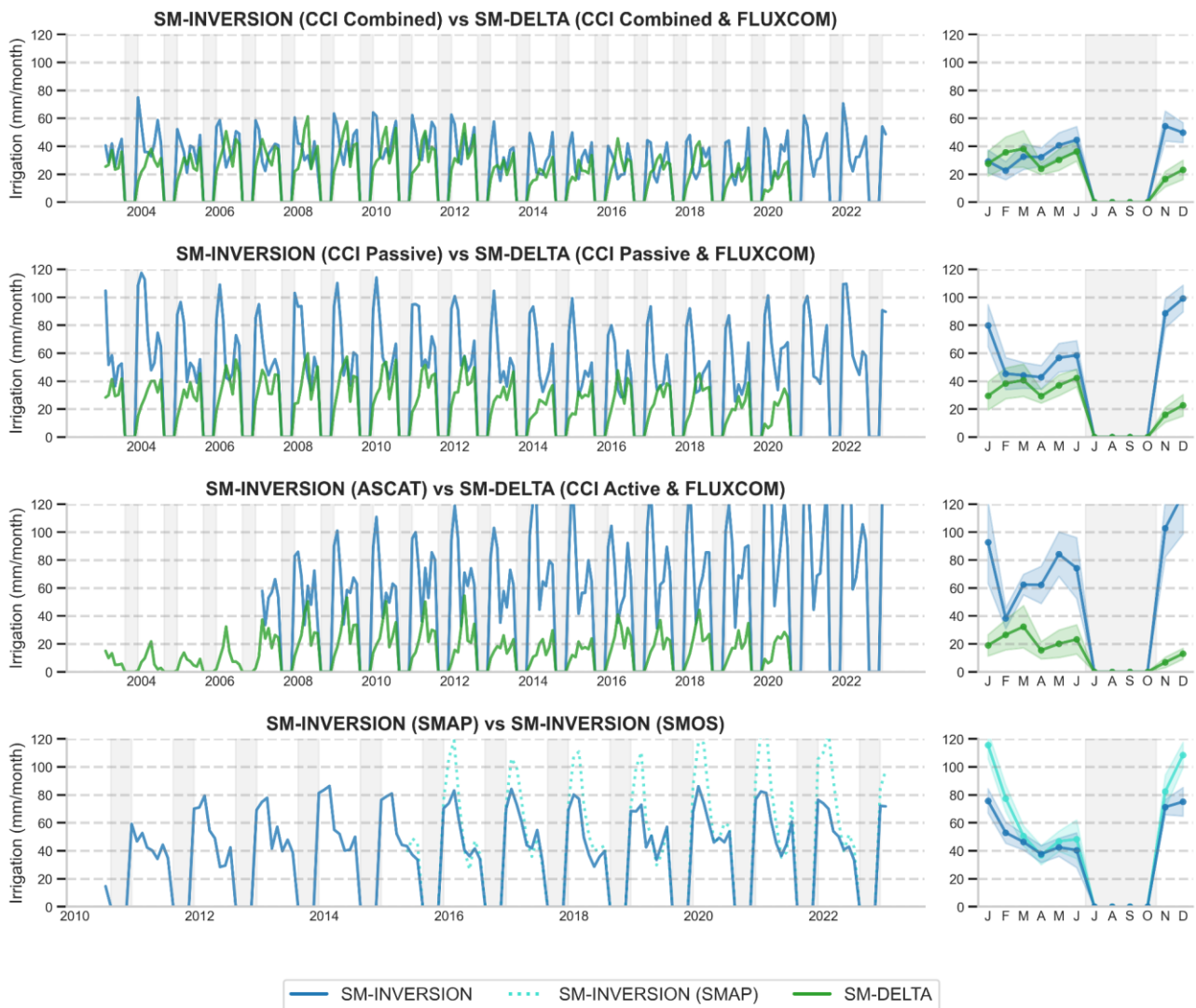


Figure 22: Monthly mean irrigation estimates from five irrigation datasets obtained with SM-INVERSION (in blue) and three datasets obtained with SM-DELTA (in green). The right panel shows the corresponding seasonal cycle. The gray shaded area corresponds to the period for which a temporal mask was applied (July to October).

6. Summary and conclusions

This study analyzes irrigation water use datasets across four regions using three methodologies: SM-DELTA, SM-INVERSION, and NOAH-MP. The similarities and differences in their performance, spatial patterns, and temporal dynamics vary across regions and methods.

CONUS

In the CONUS region, NOAH-MP datasets demonstrate the best agreement with in situ data, followed by SM-INVERSION (CCI Passive). The SM-DELTA (CCI Passive & FLUXCOM) dataset also performs well but tends to overestimate irrigation. Regarding spatial pattern, NOAH-MP (Landsat) and SM-DELTA (CCI Passive) show the highest alignment with a map of the percentage of area equipped for irrigation in the four most irrigated regions (California Valley, Snake River Plain, Mississippi Floodplain, and the Great Plains). These two datasets also capture similar temporal dynamics, including wet and dry years, despite relying on independent methodologies and input datasets.

Ebro Basin

In the Ebro basin, all datasets show an underestimation of irrigation when compared to in situ data. Metrics are relatively similar across the SM-DELTA datasets. SM-INVERSION datasets generally display stronger underestimation and lower Pearson correlations compared to SM-DELTA, with the exception of CCI Passive, which performs comparably. Regarding spatial patterns, SM-DELTA datasets exhibit some correlation with the percentage of area equipped for irrigation, whereas SM-INVERSION does not. Nevertheless, in terms of temporal dynamics, SM-DELTA (CCI Combined & FLUXCOM, CCI Passive & FLUXCOM) and SM-INVERSION (CCI Combined, CCI Passive) show strong similarities, despite differences in algorithms and input datasets.

Murray-Darling basin

In the Murray-Darling Basin, performance varies widely between districts, with no dataset consistently standing out. SM-DELTA datasets using SSEBOP ET and SM-INVERSION (CCI Passive) tend to perform better in Murrumbidgee and Coleambally, while NOAH-MP (Landsat) shows better results in Murray Mulwala and Coleambally. Regarding spatial patterns, NOAH-MP (Landsat) exhibits the strongest correlation with the percentage of area equipped for irrigation, while SM-DELTA datasets using FLUXCOM ET show only weak correlations. Other datasets do not exhibit any clear spatial relationship. In terms of temporal dynamics, SM-DELTA (CCI Passive and CCI Combined) closely aligns with SM-INVERSION (CCI Passive and CCI Combined).

India

In India, significant discrepancies appear between the three SM-DELTA and the five SM-INVERSION datasets, with SM-INVERSION datasets consistently estimating significantly higher irrigation levels over the Ganges Valley, particularly during the Rabi season (from November to April). Spatial differences also appear, as SM-DELTA datasets exhibit a correlation with the percentage of area equipped for irrigation over the Ganges Valley, while SM-INVERSION datasets do not.

Perspectives:

The analysis revealed contrasting performances across different datasets and regions, with i) varying correlations with the area equipped for irrigation, ii) overestimations or underestimations in relation to observed data, depending on the datasets and regions, and iii) temporal dynamics of the observed data that were not always well captured.

One of the main limitations of the approaches developed and analyzed here, which we identified and has often been highlighted in the literature (e.g., Zappa et al., 2022), is the ability to detect irrigation from the coarse spatial resolution SM products used, as shown in the analysis section 5.2 "Irrigation detection" of the D3 ATBD.

A solution would be to use high-resolution SM data (1 km or less) from satellites such as Sentinel-1 or CYGNSS (Clarizia et al., 2019), as has been done in recent studies with promising results (e.g., Dari et al., 2020, 2023; Zappa et al., 2021, 2024; Lalluet et al., 2024). Nevertheless, these products are usually only available after 2015, which is too recent to support the development of a robust ECV for AWU.

We suggest two main pathways for future improvement:

1. **Using higher-resolution SM data with sufficient temporal coverage:** Downscaling approaches like DISPATCH (Merlin et al., 2015), which leverage optical and thermal remote sensing observations, as well as machine learning-based methods (Zappa et al., 2019; Senanayake et al., 2024), have demonstrated the ability to refine coarse resolutions down to ~1 km while maintaining broad temporal coverage and enhancing irrigation detection (Escorihuela and Quintana-Seguí, 2016). Furthermore, the upcoming ESA CCI SM at 0.1° spatial resolution, currently in production, is also a very promising candidate to capture better irrigation signatures in SM data as well as to ensure long-term temporal coverage.
2. **Assimilating higher-resolution data in NOAH-MP:** For the NOAH-MP approach, assimilating higher-resolution SM data mentioned above, along with high-resolution ET datasets such as PMLv2 (Zhang et al., 2016), FLUXCOM (Jung et al., 2019), and SSEBop (Senay et al., 2013), could significantly improve the method's ability to detect and quantify irrigation.

Finally, exploring the links between AWU estimates, climatic events (e.g., droughts, wet years), as well as socio-economic impacts (e.g., water restrictions, shortages), would be valuable for indirectly validating our irrigation estimates.

Appendix

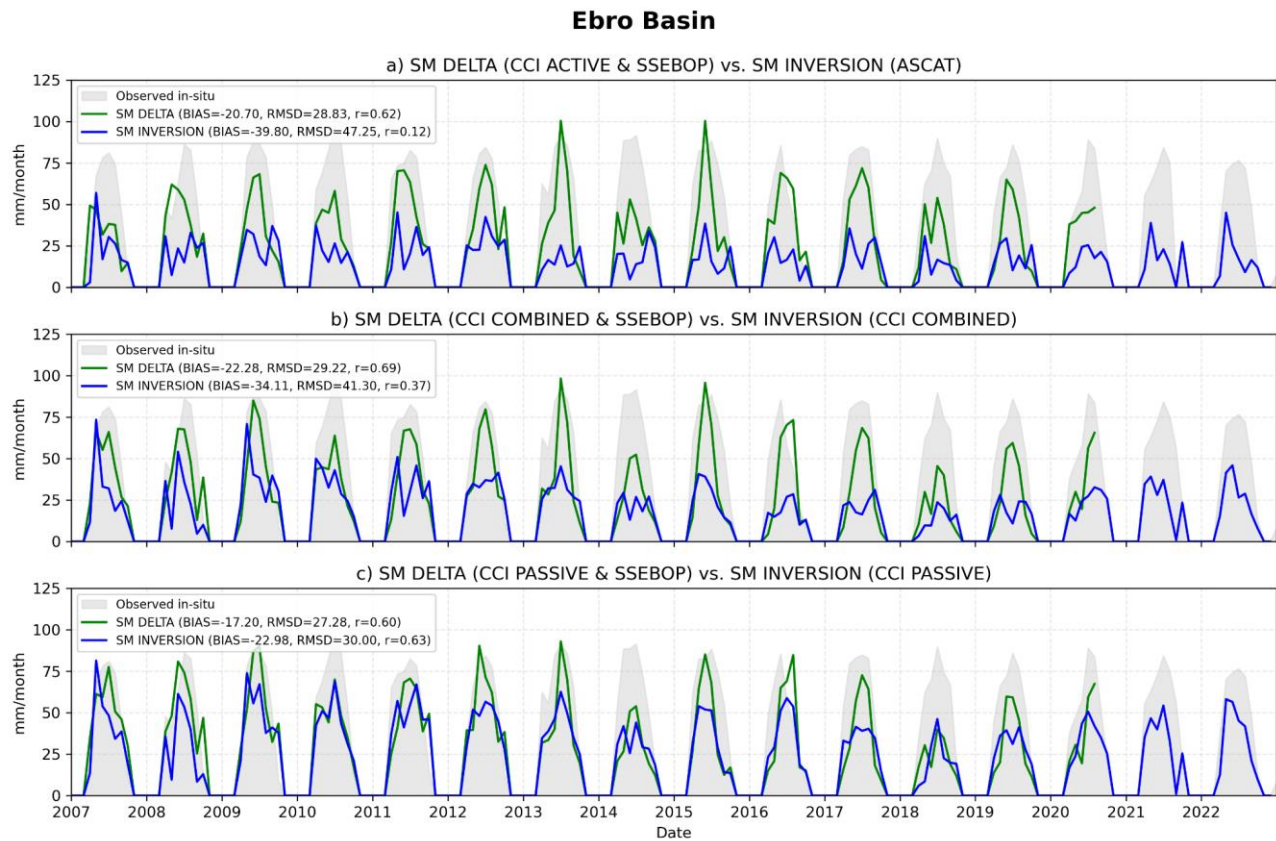


Figure A1: Average monthly irrigation over the irrigation districts of the eastern Ebro from the three SM-DELTA datasets using SSEBOP ET (green lines), three SM-INVERSION datasets (CCI Combined, CCI PASSIVE, ASCAT), along with the in situ data (grey shaded area).

Murray_Wakool (Area: 1275.0 km²)

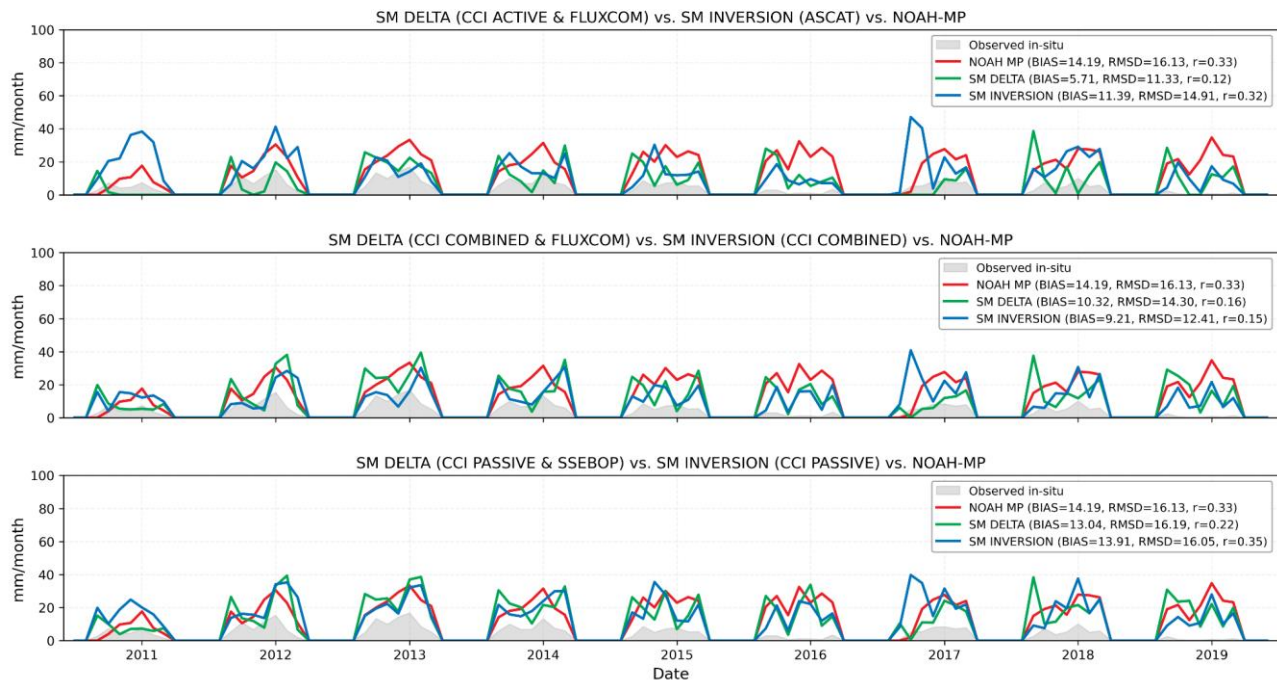


Figure A2: Average monthly irrigation over the Murray Wakool irrigation districts from three SM-DELTA datasets using FLUXCOM ET (green lines), three SM-INVERSION datasets (CCI Combined, CCI Passive, ASCAT), along with the in situ data (grey shaded area).

Murray_Mulwala (Area: 1480.0 km²)

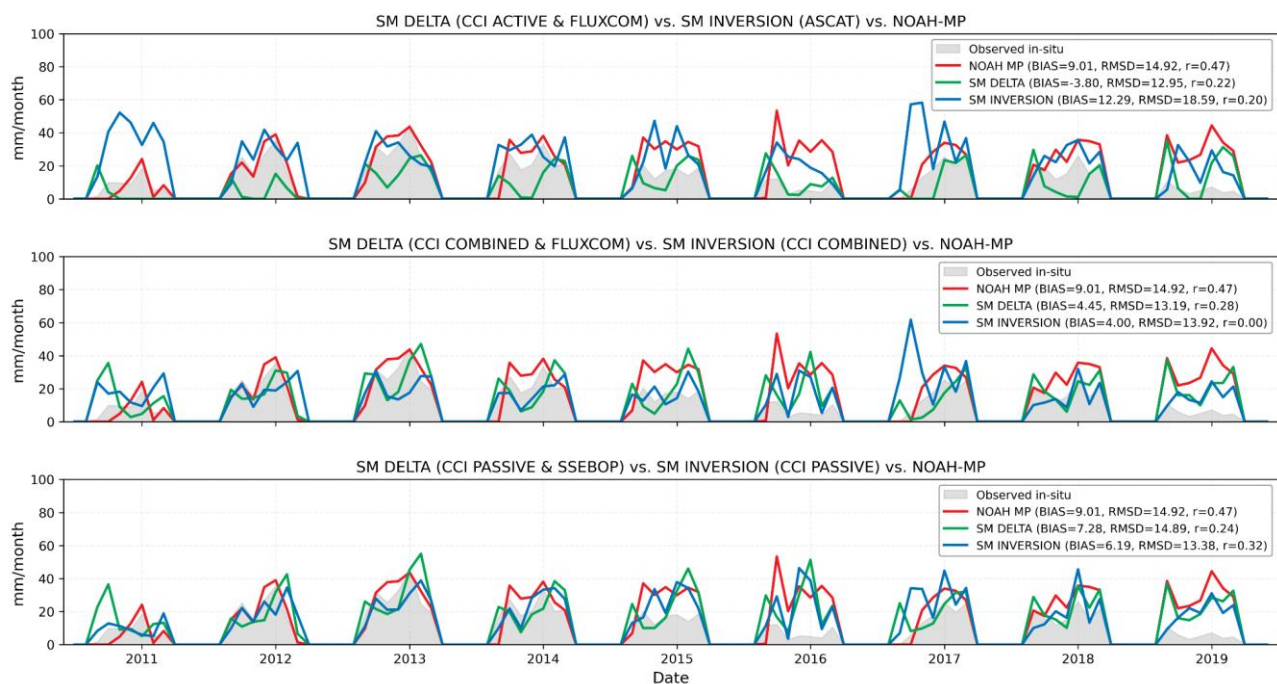


Figure A3: Same as Figure A2 but for the Murray Mulwala irrigation district.

Murrumbidgee (Area: 1600.0 km²)

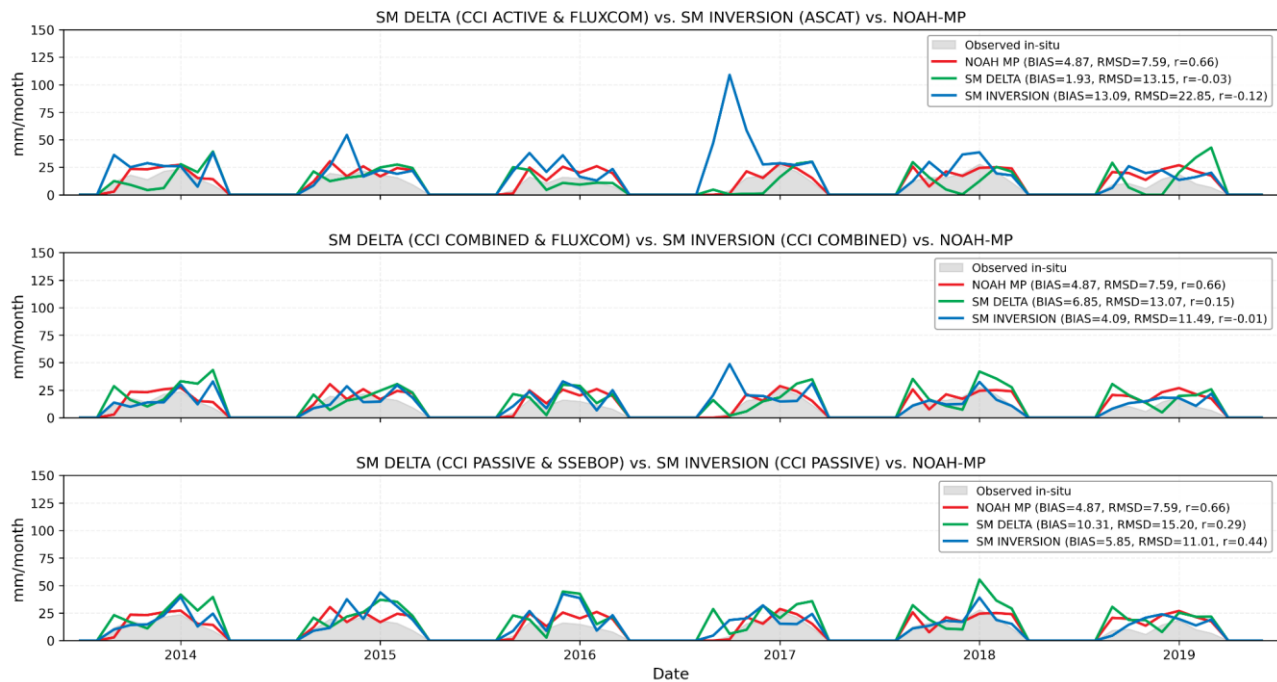


Figure A4: Same as Figure A2 and A3 but for the Murrumbidgee irrigation district.

Coleambally (Area: 977.0 km²)

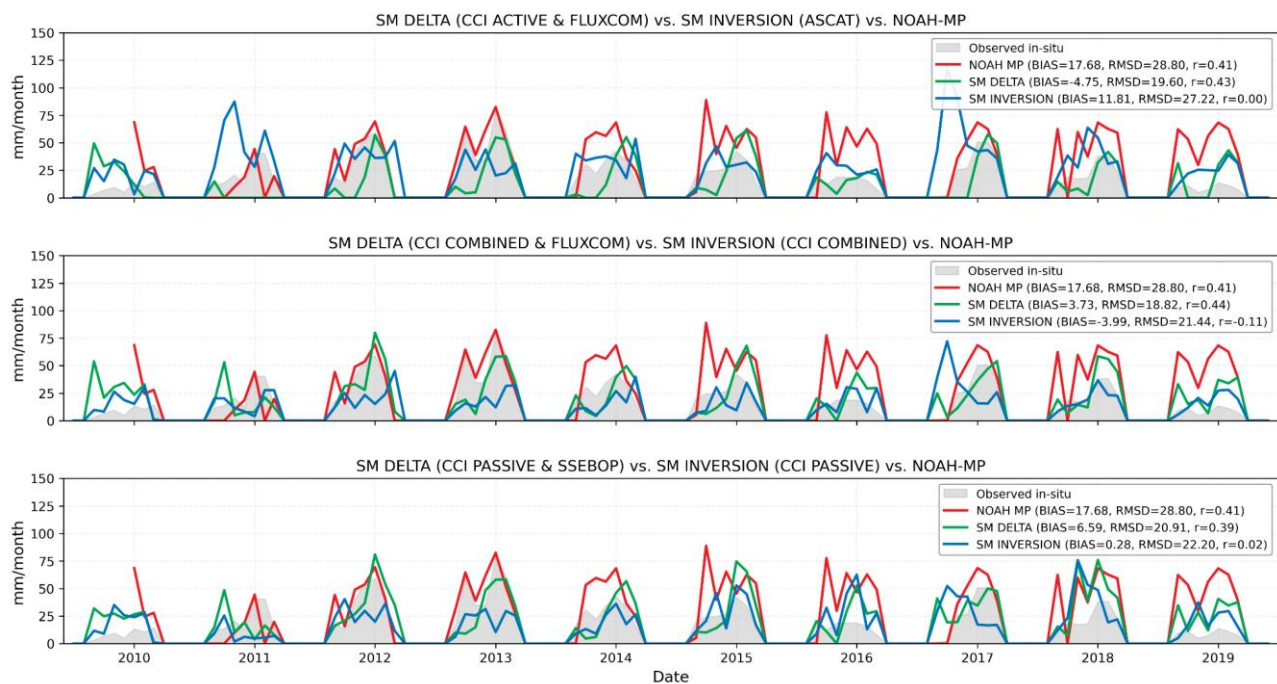


Figure A5: Same as Figures A2, A3, and A4 but for the Coleambally irrigation district.

References

- Blunden, J., Arndt, D.S., Baringer, M.O., 2011. State of the Climate in 2010. Bulletin of the American Meteorological Society 92, S1–S236. <https://doi.org/10.1175/1520-0477-92.6.S1>
- Brocca, L., Tarpanelli, A., Filippucci, P., Dorigo, W., Zaussinger, F., Gruber, A., Fernández-Prieto, D., 2018. How much water is used for irrigation? A new approach exploiting coarse resolution satellite soil moisture products. International Journal of Applied Earth Observation and Geoinformation 73, 752–766. <https://doi.org/10.1016/j.jag.2018.08.023>
- Clarizia, M.P., Pierdicca, N., Costantini, F., Floury, N., 2019. Analysis of CYGNSS Data for Soil Moisture Retrieval. IEEE Journal of Selected Topics in Applied Earth Observations and Remote Sensing 12, 2227–2235. <https://doi.org/10.1109/JSTARS.2019.2895510>
- Dari, J., Brocca, L., Modanesi, S., Massari, C., Tarpanelli, A., Barbetta, S., Quast, R., Vreugdenhil, M., Freeman, V., Barella-Ortiz, A., Quintana-Seguí, P., Breitreger, D., Volden, E., 2023. Regional data sets of high-resolution (1 and 6 km) irrigation estimates from space. Earth System Science Data 15, 1555–1575. <https://doi.org/10.5194/essd-15-1555-2023>
- Dari, J., Brocca, L., Quintana-Seguí, P., Escorihuela, M.J., Stefan, V., Morbidelli, R., 2020. Exploiting High-Resolution Remote Sensing Soil Moisture to Estimate Irrigation Water Amounts over a Mediterranean Region. Remote Sensing 12, 2593. <https://doi.org/10.3390/rs12162593>
- Dari, J., Quintana-Seguí, P., Morbidelli, R., Saltalippi, C., Flammini, A., Giugliarelli, E., Escorihuela, M.J., Stefan, V., Brocca, L., 2022. Irrigation estimates from space: Implementation of different approaches to model the evapotranspiration contribution within a soil-moisture-based inversion algorithm. Agricultural Water Management 265, 107537. <https://doi.org/10.1016/j.agwat.2022.107537>
- van Dijk, A.I.J.M., Beck, H.E., Crosbie, R.S., de Jeu, R.A.M., Liu, Y.Y., Podger, G.M., Timbal, B., Viney, N.R., 2013. The Millennium Drought in southeast Australia (2001–2009): Natural and human causes and implications for water resources, ecosystems, economy, and society. Water Resources Research 49, 1040–1057. <https://doi.org/10.1002/wrcr.20123>
- Dorigo, W., Wagner, W., Albergel, C., Albrecht, F., Balsamo, G., Brocca, L., Chung, D., Ertl, M., Forkel, M., Gruber, A., Haas, E., Hamer, P.D., Hirschi, M., Ikonen, J., de Jeu, R., Kidd, R., Lahoz, W., Liu, Y.Y., Miralles, D., Mistelbauer, T., Nicolai-Shaw, N., Parinussa, R., Pratola, C., Reimer, C., van der Schalie, R., Seneviratne, S.I., Smolander, T., Lecomte, P., 2017. ESA CCI Soil Moisture for improved Earth system understanding: State-of-the art and future directions. Remote Sensing of Environment, Earth Observation of Essential Climate Variables 203, 185–215. <https://doi.org/10.1016/j.rse.2017.07.001>
- Escorihuela, M.J., Quintana-Seguí, P., 2016. Comparison of remote sensing and simulated soil moisture datasets in Mediterranean landscapes. Remote Sensing of Environment, Special Issue: ESA's Soil Moisture and Ocean Salinity Mission - Achievements and Applications 180, 99–114. <https://doi.org/10.1016/j.rse.2016.02.046>

-
- Jung, M., Koirala, S., Weber, U., Ichii, K., Gans, F., Camps-Valls, G., Papale, D., Schwalm, C., Tramontana, G., Reichstein, M., 2019. The FLUXCOM ensemble of global land-atmosphere energy fluxes. *Sci Data* 6, 74. <https://doi.org/10.1038/s41597-019-0076-8>
- Kragh, S.J., Fensholt, R., Stisen, S., Koch, J., 2023. The precision of satellite-based net irrigation quantification in the Indus and Ganges basins. *Hydrology and Earth System Sciences* 27, 2463–2478. <https://doi.org/10.5194/hess-27-2463-2023>
- Kumar, S.V., Peters-Lidard, C.D., Tian, Y., Houser, P.R., Geiger, J., Olden, S., Lighty, L., Eastman, J.L., Doty, B., Dirmeyer, P., Adams, J., Mitchell, K., Wood, E.F., Sheffield, J., 2006. Land information system: An interoperable framework for high resolution land surface modeling. *Environmental Modelling & Software* 21, 1402–1415. <https://doi.org/10.1016/j.envsoft.2005.07.004>
- Laluet, P., Olivera-Guerra, L.E., Altés, V., Paolini, G., Ouadi, N., Rivalland, V., Jarlan, L., Villar, J.M., Merlin, O., 2024. Retrieving the irrigation actually applied at district scale: Assimilating high-resolution Sentinel-1-derived soil moisture data into a FAO-56-based model. *Agricultural Water Management* 293, 108704. <https://doi.org/10.1016/j.agwat.2024.108704>
- Merlin, O., Escorihuela, M.J., Mayoral, M.A., Hagolle, O., Al Bitar, A., Kerr, Y., 2013. Self-calibrated evaporation-based disaggregation of SMOS soil moisture: An evaluation study at 3 km and 100 m resolution in Catalunya, Spain. *Remote Sensing of Environment* 130, 25–38. <https://doi.org/10.1016/j.rse.2012.11.008>
- Ozdogan, M., Rodell, M., Beaudoin, H.K., Toll, D.L., 2010. Simulating the Effects of Irrigation over the United States in a Land Surface Model Based on Satellite-Derived Agricultural Data. *Journal of Hydrometeorology* 11, 171–184. <https://doi.org/10.1175/2009JHM1116.1>
- New South Wales Government., 2024. The 2017-20 drought. NSW Government Water. URL <https://water.dpie.nsw.gov.au/our-work/allocations-availability/drought-and-floods/drought-recovery/2017-20-drought> (accessed 3.4.25).
- Senanayake, I.P., Pathira Arachchilage, K.R.L., Yeo, I.-Y., Khaki, M., Han, S.-C., Dahlhaus, P.G., 2024. Spatial Downscaling of Satellite-Based Soil Moisture Products Using Machine Learning Techniques: A Review. *Remote Sensing* 16, 2067. <https://doi.org/10.3390/rs16122067>
- Senay, G.B., Bohms, S., Singh, R.K., Gowda, P.H., Velpuri, N.M., Alemu, H., Verdin, J.P., 2013. Operational Evapotranspiration Mapping Using Remote Sensing and Weather Datasets: A New Parameterization for the SSEB Approach. *JAWRA Journal of the American Water Resources Association* 49, 577–591. <https://doi.org/10.1111/jawr.12057>
- Siebert, S., Henrich, V., Frenken, K., Burke, J., 2013. Update of the digital global map of irrigation areas to version 5. <https://doi.org/10.13140/2.1.2660.6728>
- Teluguntla, P., Thenkabail, P., Oliphant, A., Gumma, M., Aneece, I., Foley, D. and McCormick, R. (2023). Landsat-derived Global Rainfed and Irrigated-Cropland Product @ 30-m (LGRIP30) of the World (GFSADLGRIP30WORLD). The Land Processes Distributed Active Archive Center (LP DAAC) of NASA and USGS. Pp. 103. IP-148728. DOI: <https://doi.org/10.5067/Community/LGRIP/LGRIP30.001>

Zhang, Y., Peña-Arancibia, J.L., McVicar, T.R., Chiew, F.H.S., Vaze, J., Liu, C., Lu, X., Zheng, H., Wang, Y., Liu, Y.Y., Miralles, D.G., Pan, M., 2016. Multi-decadal trends in global terrestrial evapotranspiration and its components. *Sci Rep* 6, 19124. <https://doi.org/10.1038/srep19124>

Zappa, L., Dari, J., Modanesi, S., Quast, R., Brocca, L., De Lannoy, G., Massari, C., Quintana-Seguí, P., Barella-Ortiz, A., Dorigo, W., 2024. Benefits and pitfalls of irrigation timing and water amounts derived from satellite soil moisture. *Agricultural Water Management* 295, 108773. <https://doi.org/10.1016/j.agwat.2024.108773>

Zappa, L., Schlaffer, S., Bauer-Marschallinger, B., Nendel, C., Zimmerman, B., Dorigo, W., 2021. Detection and Quantification of Irrigation Water Amounts at 500 m Using Sentinel-1 Surface Soil Moisture. *Remote Sensing* 13, 1727. <https://doi.org/10.3390/rs13091727>

Zappa, L., Schlaffer, S., Brocca, L., Vreugdenhil, M., Nendel, C., Dorigo, W., 2022. How accurately can we retrieve irrigation timing and water amounts from (satellite) soil moisture? *International Journal of Applied Earth Observation and Geoinformation* 113, 102979. <https://doi.org/10.1016/j.jag.2022.102979>